

Investigation of the characteristics of low-level jets over North America in a convection-permitting WRF simulation

Xiao Ma^{1,2}, Yanping Li^{1,2}, Zhenhua Li¹, Fei Huo¹

¹Global Institute for Water Security, University of Saskatchewan, 11 Innovation Blvd, Saskatoon, SK, S7N 3H5, Canada

²School of Environment and Sustainability, University of Saskatchewan, 117 Science Place, Saskatoon, SK, S7N 5C8, Canada

Correspondence to: Yanping Li (yanping.li@usask.ca)

Abstract. In this study, we utilized a high-resolution (4 km) convection-permitting Weather Research Forecasting (WRF) simulation spanning a 13-year period (2000-2013) to investigate the climatological features of Low-level Jets (LLJs) over North America. The 4-km simulation enabled us to represent the effects of orography and the underlying surface on the boundary layer winds better. Focusing on the continental US and the adjacent border regions of Canada and Mexico, this study not only identified several well-known large-scale LLJs, such as the southerly Great Plains LLJ and the summer northerly California coastal LLJ, but also the winter Quebec northerly LLJ which gets less focus before. All these LLJs reach the strongest in the night time in the diurnal cycle. Thus, the different thermal and dynamic mechanisms forming these three significant LLJs are investigated in this paper: Inertial oscillation theory dominates in Great Plain LLJ, California coastal LLJ is formed by the baroclinic theory, whereas the Quebec LLJ is associated with both theories. Moreover, the high-resolution simulation revealed climatic characteristics of weaker and smaller-scale LLJs or low-level wind maxima in regions with complex terrains, such as the northerly LLJs in the foothill regions of the Rocky Mountains and the Appalachian during the winter. This study provides valuable insights into the climatological features of LLJs in North America and the high-resolution simulation offers a more detailed understanding of LLJ behavior near complex terrains and other smaller-scale features.

删除了: climatology

删除了: high-resolution

删除了: characterizes the spatial distribution, seasonal patterns, and diurnal fluctuations of northerly/southerly LLJ occurrence frequencies. This paper

删除了: in North America,

删除了: Quebec northerly LLJ, which gets less focus before.

删除了: Additionally, the different thermal and dynamic mechanisms forming significant LLJs near the Great Plains, California, and Quebec are investigated.

删除了:

36 **1. Introduction**

37 A low-level jet (LLJ) is described as the fast-moving air ribbon located in the lower atmosphere most of the time
38 (Bonner, 1968; Rife et al., 2010). Many of the world's LLJs have been studied, such as the Great Plains LLJ over the
39 central US (Bonner, 1968; Zhong et al., 1996), the Somali LLJ over eastern Africa (Munday et al., 2021), and the
40 South American LLJ over the east Andes Mountains (Montini et al., 2019). Other studies extend beyond in-land LLJs
41 to encompass offshore coastal LLJs such as the California LLJs (Parish, 2000) and North African Coastal LLJ (Soares
42 et al., 2018). A kind of mesoscale weather system, an LLJ has a relatively small vertical range of usually only a few
43 hundred meters, but its width can reach several hundred kilometers. LLJs are closely related to precipitation and even
44 extreme events, and they can transfer abundant water vapor to the downwind regions, providing favorable dynamic
45 conditions for rainfall (Walters and Winkler, 2001; Hodges and Pu, 2019). Meanwhile, researchers have long been
46 interested in investigating their features, because LLJs also affect various processes such as wind power development,
47 air pollution transportation, and urban heat islands; the wind turbines would be influenced by positive wind shear and
48 downward entrainment from the LLJs above them, assisting in extracting energy from the strong wind belt inside LLJs
49 (Gadde and Stevens 2021; Ma et al., 2022). LLJ-related horizontal transportation is beneficial to pollutant removal
50 (Sullivan et al. 2017). The LLJs can enhance the turbulent mixing in the boundary layer thereby decreasing the
51 atmospheric stability, helping pollution diffusion, and weakening urban heat island intensity (Hu et al., 2013).

52 Since the mid-20th century, scientists have used regular rawinsonde observations to investigate the characteristics of
53 LLJs. Applying rawinsondes to investigate the Great Plains LLJ in the central US, Bonner (1968), Mitchell et al.
54 (1995), and Walters et al. (2008) studied its distribution, seasonal activity, horizontal and vertical structure, and diurnal
55 features and established the climatology of the Great Plains LLJ during warm seasons. As well as rawinsondes, radar
56 systems and wind profilers are useful tools for characterizing LLJs. Frisch et al. (1992) observed a typical LLJ process
57 using Doppler weather radar in North Dakota and identified that the friction on the surface of the boundary layer is
58 important in the early stages of LLJ development. Using long-term wind profiler measurement, Miao et al. (2018)
59 interpreted the climatology of LLJs in Beijing and Guangzhou, concluding that the frequency values of LLJs in these
60 two cities are 13.0% and 4.9%, respectively. Moreover, Smith et al. (2019) used the Plains Elevated Convection at
61 Night (PECAN) observations to conduct high-quality measurements of nocturnal LLJs with wide spatial and temporal
62 resolutions. They found that sudden changes in LLJ structure typically result from the spatial evolution of the LLJ.

删除了: generally

删除了: Because

删除了: (Hu et al., 2013; Sullivan et al. 2017;

删除了: , Ma et al., 2022), researchers have long been interested in investigating their features.

68 However, there are some disadvantages of observational research that should be noted. First, regular rawinsonde data
69 only contain measurements at two daily time points (00 UTC and 12 UTC), which cannot fully capture LLJs' diurnal
70 variations. The time density of observations is therefore coarse, and coastal areas lack regular high-density
71 measurements, making the study of coastal LLJs challenging (Mitchell et al., 1995). Second, heterogeneities in the
72 rawinsonde records, such as variations in station locations, radiosonde types, and archiving procedures, may also
73 complicate the use of these observations in climate research. Third, rawinsonde measurements taken at a single point
74 are not able to capture horizontal shear and environmental conditions (Chen et al., 2005). Although ~~observation~~
75 platforms such as radar, PECAN, ~~or lidar which investigate the atmosphere as low as 300 m~~, can compensate to some
76 extent for this lack of observational data, ~~as well as lidar that investigates the atmosphere as low as 300 m~~, these
77 approaches are still limited by the spatial coverage of their measurement platforms (Smith et al., 2019).

78 Because of these problems with observational methods, researchers have chosen reanalysis datasets as an alternative
79 for investigating LLJs. Reanalysis data have relatively better spatial and temporal coverage than rawinsonde
80 measurements, incorporate observations into the preliminary model simulations, ~~provide more comprehensive~~
81 ~~variables through assimilation~~, and contain broader domains. Rife et al. (2010) highlighted the global distribution of
82 identified nocturnal LLJs using reanalysis data with a horizontal grid spacing of 40 km, and even successfully
83 extracted some previously unknown jets, ~~like Tarim nocturnal LLJ in northwest China, Ethiopia nocturnal LLJ, and~~
84 ~~Namibia–Angola nocturnal LLJ~~. Doubler et al. (2015) applied the North American Regional Reanalysis (NARR)
85 dataset (~32 km) to generate long-term LLJ climatology in North America. Consistent with previous records,
86 Doubler's results supplemented the description of some smaller-scale LLJs. Similarly, Montini et al. (2019) compared
87 and validated the performance of five different reanalysis datasets in identifying LLJs. Their results showed the 38-
88 year climatology of South American LLJs with ERA-Interim data (~79 km).

89 Scientists have also conducted studies based on numerical simulations, which can more accurately represent LLJs than
90 reanalysis data sets, especially in the vertical direction, thereby yielding new insights into LLJs' features. Tang et al.
91 (2017) used an ensemble of dynamically downscaling regional climate simulations to generate the climatology of
92 Great Plains LLJ and predicted that the LLJ will occur more frequently during the nighttime in spring and summer in
93 mid-21st century. Jiménez-Sánchez et al. (2019) conducted a simulation for LLJs over the Orinoco River Basin by
94 dynamic downscaling of the Weather Research and Forecasting model (WRF). The simulation represented the jet

删除了: observations

删除了: or field projects like

删除了:

删除了: perform more extensive measurements

删除了: .

100 streaks better than previous studies within a broader region of wind enhancement and illustrated more detailed diurnal
101 evolution. Nevertheless, most general numerical simulations still represent the convective processes by the
102 parameterization scheme, which generates uncertainty in the results. These issues can be addressed by using
103 convection-permitting models with grid spacing under 5 km that adequately simulate the convections and other small-
104 scale processes (Liu et al., 2017, Li et al., 2019, Kurkute et al., 2020). Convection-permitting modeling describes the
105 underlying surface more accurately than coarse-resolution simulations and reanalysis data and shows ability in
106 investigations of LLJs near complex mountain areas. Du and Chen (2019) analyzed the LLJs over southern China by
107 using 4-km WRF model and revealed a solid relationship between the mesoscale lifting of LLJs and the convection's
108 initiation. They also highlighted the importance of coastal terrain. Overall, the finer-resolution tools tend to show more
109 comprehensive and precise results, offering detailed and accurate references to LLJs.

110 The formation mechanisms of LLJs have been studied extensively by researchers. In explaining the diurnal cycle
111 feature of the Great Plains LLJ, the inertial oscillation theory proposed by Blackadar (1957) and Stensrud (1996)
112 suggests that the LLJ is related to the friction change in the boundary layer. During the night, the jet-core wind is
113 enhanced after decoupling with near-surface friction. Holton (1967) and Parish (2000) developed the thermal wind
114 adjustment theory, which suggests that the horizontal pressure gradient changes because the atmosphere over sloping
115 terrain is warmer or because sea-land contrast influences the diurnal cycle of wind. Additionally, LLJs can also be
116 formed due to synoptic system forcing, as proposed by Uccellini et al. (1987) and Saulo et al. (2007). However,
117 convection-permitting models can help explain how LLJs form because they have precise descriptions of weather
118 systems and underlying orography. Using 4-km simulations, Fu et al. (2018) and Zhang et al. (2019) analyzed the
119 evolution of LLJs over mountainous areas in eastern and southwestern China, respectively. They concluded that
120 inertial oscillation plays a prominent role in and is responsible for the local precipitation peak at a certain time. Besides,
121 Shapiro et al. (2016) argued that the formation of some LLJs may not be impacted by a single factor and that a unified
122 theory analysis is thus required. Thus, a dataset that offers more information must be very popular. All these studies
123 have shown that convection-permitting models, with both finer coverage and resolutions, are a powerful tool for LLJ
124 characteristics research.

125 In this study, we utilize the 4-km convection-permitting WRF simulation (Liu et al., 2017) to analyze the features of
126 low-level jet systems across North America, improving the spatial and temporal resolutions. Section 2 introduces the

删除了: promise

删除了: In

删除了:), it is suggested

删除了: diurnal cycle feature of the Great Plains LLJ

删除了: climatology

删除了: The purpose of

删除了: is to use

删除了: model

删除了: produce a detailed LLJ climatology. This paper focuses on...

删除了: LLJs in major areas of

删除了: and aims to provide alternative dataset sources with...

删除了: finer

删除了: resolution for the LLJs in this region and provide more helpful tools for LLJs-related studies in other disciplinary...

144 model configuration and the criteria for LLJ identification, Section 3 presents the characteristics of LLJ frequencies
145 in North America, and Section 4 illustrates the analysis of the background and mechanisms in several LLJ cases.
146 Finally, Section 5 provides the discussion and conclusion.

147 2. Model configuration and methods

148 2.1 WRF setup

149 This study utilized a convection-permitting Weather Research and Forecasting (WRF) dataset (Liu et al. 2017, Data
150 available at: <https://rda.ucar.edu/datasets/ds612.0/>) with a horizontal resolution of 4 km over North America, ~~without~~
151 ~~nesting~~. The domain covers the entire continental US, Southern Canada, and Northern Mexico, as illustrated in Figure
152 1. The simulation provides three-dimensional data at a temporal resolution of 3 hours, resulting in 8-time steps per
153 day. In the vertical direction, the data have 51 eta levels and can reach 50 hPa. ~~It~~ should be noted that there are five
154 layers under 500-m height and nine layers under 1 km are outputted above ground level, which means the WRF has ~~a~~
155 ~~better~~ ability ~~than other coarse modelling~~, to capture the LLJs occurring in the boundary layer. ~~Considering the~~
156 ~~computational cost for high-resolution modelling, this~~ simulation period spans from 1st October 2000 to 30th
157 September 2013, and the six-hourly ERA-Interim reanalysis dataset of 0.7° resolution was used as input for the climate
158 simulation, ~~the vertical layer depth of the forcing ERA-Interim data under 5 km is about 0.3-1.4 km (Hoffmann &~~
159 ~~Spang, 2022)~~. It is noted that 13 years is shorter than the normally defined climatology, but considering the
160 ~~computational cost of high-resolution simulation, it is still a balanced compromise. This shorter period length was also~~
161 ~~utilized to analyze the climate features of other weather events (Liu et al., 2017, Li et al., 2019)~~. The simulation did
162 not apply any cumulus parameterization scheme due to the fine horizontal grid spacing, but other sub-grid scale
163 processes were parameterized by various physical schemes: the rapid radiative transfer model (RRTMG) (Iacono et
164 al., 2008) was used for simulating longwave and shortwave radiations, the Yonsei University (YSU) scheme was used
165 for representing the planetary boundary layer (Hong et al., 2006), and the Noah-MP model was used for computing
166 surface processes (Niu et al., 2011). In this study, the planetary boundary layer scheme is retained, ~~Nonetheless~~, it
167 should be noted that this would introduce uncertainties to the simulation in the vertical direction, especially in regions
168 with complex topography. ▲

删除了: .

删除了: And it

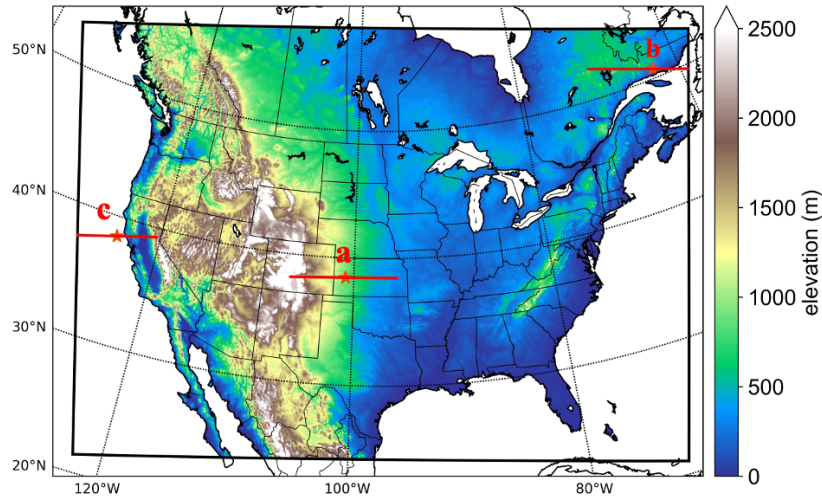
删除了: the good

删除了: The

删除了: .

删除了: , but

设置了格式



175
 176 **Figure 1. Study domain of this convection-permitting model. The colors represent the elevation. The red lines and stars**
 177 **show the positions of investigated cross-section and jets in Section 4.**

178

179 **2.2 Methodology**

180 Using the threshold criteria proposed by Bonner (1968), this study identifies LLJs from the vertical wind profile of
 181 each grid point in the model output data. LLJs are present when the following conditions are met: (1) the height of the
 182 LLJ core maximum wind speed is below 3 km above the ground level (AGL); (2) the maximum wind speed is greater
 183 than or equal to 12 m s⁻¹; (3) from the height of the wind maxima to the height of the next minimum value or 3-km
 184 height (whichever is lower), the velocity of winds drop by at least 6 m s⁻¹; (4) the wind speed drops by at least 6 m s⁻¹
 185 1 below the level of wind maxima. Considering the importance of the meridional LLJ for heat and water vapor
 186 transport, this study addresses their frequencies in different meridional directions. According to Walter et al. (2008)
 187 and Doubler et al. (2015), the criteria for identifying different meridional LLJs are as follows: for southerly LLJs (S-
 188 LLJs), the jet-core wind direction is between 113° and 247°; for northerly LLJs (N-LLJs), the jet-core direction is
 189 between 293° and 67°. These criteria are used in this study.

190 Based on the identification criteria above, we determined if the LLJ existed at each grid point and consequently
 191 counted the occurrences of S-LLJs and N-LLJs. We also calculated the frequencies of LLJs in different seasons or

192 time steps. The frequency is defined as the percentage of the total number of occurrences for the selected accumulation
193 period. We generated the frequency distribution maps for LLJs in North America, which are illustrated in Section 3.

删除了: climatology

194 3. The patterns of North American LLJs

删除了: climatology

195 3.1 Analysis of atmospheric circulation

196 This study adopts model data to capture the climatological features of LLJs in North America. Considering the
197 relationship between LLJs and synoptical systems, we evaluated the ability of the convection-permitting model to
198 simulate the background atmospheric circulation. Figure 2 depicts the simulated multi-year analysis of geopotential
199 heights at 500 hPa and sea-level pressure isobars for summer and winter. In summer, at a height of 500 hPa (Figure
200 2a), In summer, the model depicts a trough in the east of the continental US, a ridge over the Rocky Mountains, and
201 the upper-air subtropical anticyclone crossing the southern US. At sea level (Figure 2b), the model captures the Azores
202 High-Pressure area in the Atlantic Ocean and the Hawaiian High-Pressure area in the Pacific.

删除了: climatology

203 In winter, the contours at the pressure value of 500 hPa (Figure 2c) show stronger fluctuating characteristics: the
204 eastern trough and western ridge over the continent strengthen, and the polar vortex extends to the northern US, while
205 most of North America is controlled by a cold high-pressure system. In addition, the subtropical anticyclone is too
206 weak to be found within the study domain. On the other hand, most of North America is controlled by a cold high-
207 pressure system at sea level (Figure 2d), and parts of the Icelandic Low and Aleutian Low appear on both east and
208 west of Canada, even though their centers are not captured in the domain. To summarize, the convection-permitting
209 model can simulate the features of semi-permanent centers of atmospheric circulations in North America, thus
210 demonstrating its strength in identifying the LLJs in this area.

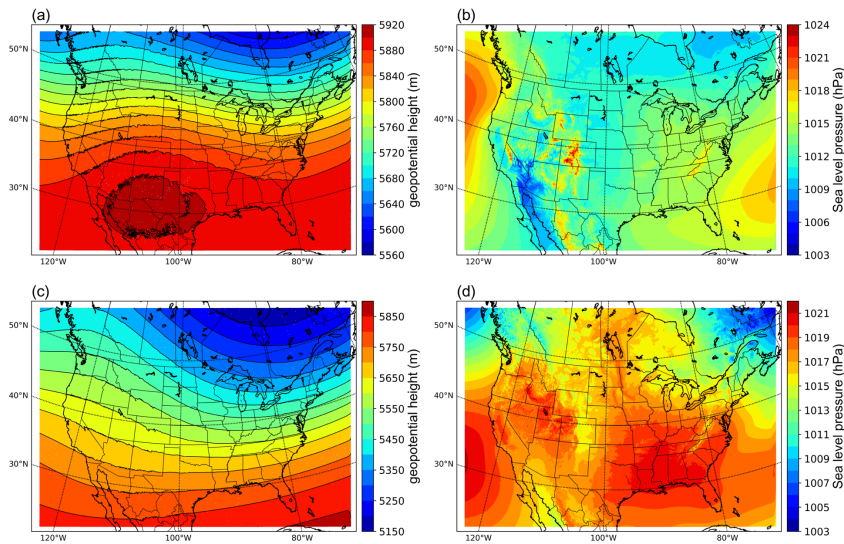
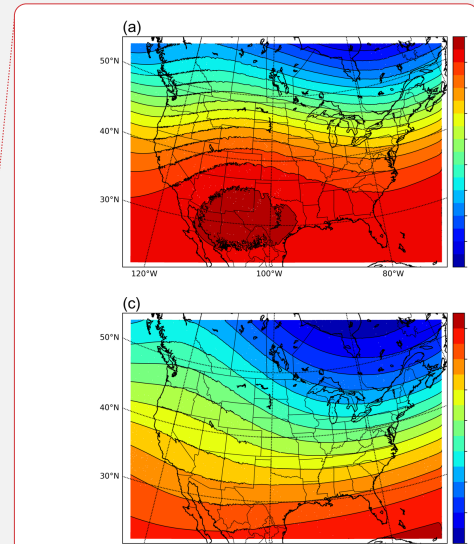


Figure 2. Multi-year patterns of atmospheric circulations simulated by the convection-permitting model: (a) summer 500 hPa geopotential height; (b) sea-level pressure in summer; (c-d) the same variables but in winter.

3.2 Seasonal variations of LLJs

3.2.1 Northerly LLJs

Figure 3 illustrates the seasonal frequency distribution of Northern Low-Level Jets (N-LLJs). The frequency is defined as the ratio of the total number of LLJ occurrences to the total number of time steps in each season. Notably, the California coastal LLJ peaks during the summer months (June, July, and August (JJA)), where frequencies exceed 25% over a broad area stretching from the southern Oregon coast to central California. In these regions, frequencies above 5% can even extend into the Pacific Ocean near northern Baja California. However, transitioning from summer to autumn (September, October, and November (SON)), there is a sharp decline in the frequency of this LLJ, dropping to only 5%-15% within the core region, predominantly along the northern California coast. In winter (December, January, and February (DJF)), occurrences are sparse, at approximately 1%-2%. Conversely, various N-LLJ phenomena are more prevalent during the colder seasons. These jets primarily occur near the eastern slopes of significant terrains such as the Rocky Mountains, Appalachian Mountains, and the Quebec



删除了:

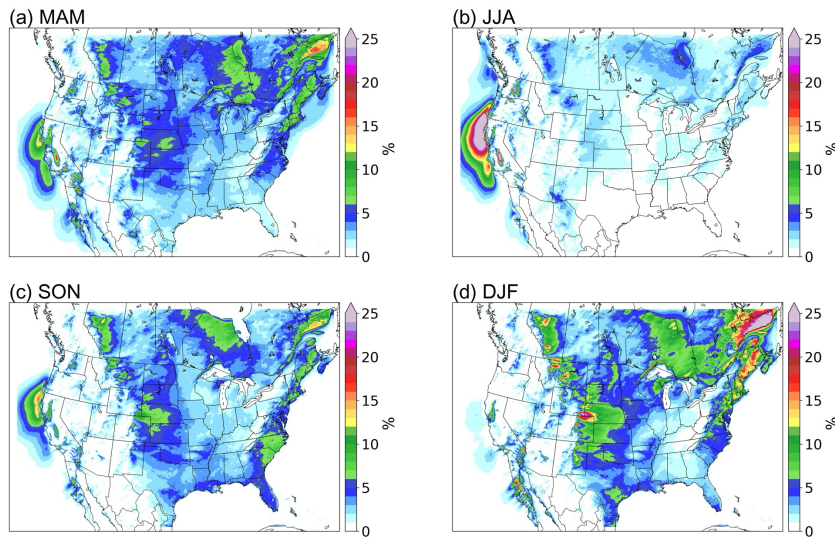
删除了: Climatology

删除了: shows...illustrates the seasonal frequency distribution of Northern Low-Level Jets (N-LLJ in four seasons, in which the ...LLJs). The frequency represents...s defined as the ratio between...f the seasonal ...total number of LLJs occurrence and...LJ occurrences to the total number of time steps in each season. Clearly...otably, the California coastal LLJ is strongest in ...eaks during the summer months (June, July, and August (JJA)), with ...here frequencies exceed 25% over a large...road area of N-LLJ frequency greater than 25%, extending...tretching from the southern Oregon coast to the ...entral California coast. Regions with a frequency greater than ... In these regions, frequencies above 5% can even extend to...nto the Pacific Ocean near northern Baja California. However, transitioning from summer to autumn (September, October, and November (SON)), there is a sharp decline in the frequency of this LLJ decrease...

删除了: On the other hand...onversely, various N-LLJ phenomena occur frequently in...re more prevalent during the cold season...older seasons. These N-LLJs are mainly located ...ets primarily occur near the eastern slopes of special...

302 Labrador Plateau. High frequencies (>10%) are observed from western Alberta to Oklahoma, during winter, with hot
 303 spots sporadically located in Alberta, Montana, Wyoming, and Colorado, where frequencies reach about 20%,
 304 particularly between Colorado and Wyoming. In more than 25% of the wind profiles analyzed, N-LLJs were
 305 identifiable. Along the Eastern US coast, N-LLJs predominantly stretch from Maine to South Carolina, with peak
 306 frequencies of approximately 15%-20%. In eastern Quebec, N-LLJs are most frequent in winter, exceeding 25%. The
 307 simulation also detects the presence of N-LLJ in about 10% of the time steps over Hudson Bay. Notably, the
 308 frequencies of all aforementioned N-LLJs significantly diminish in spring, becoming scarcely detectable in summer
 309 with frequencies mostly under 5%.

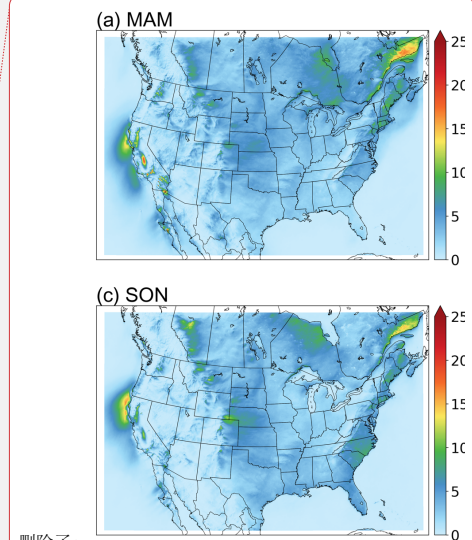
删除了： In winter, high...igh frequencies (>10%) are
 observed from western Alberta to Oklahoma, within
 which ...during winter, with hot spots are
 distributed ...poradically located in Alberta, Montana,
 Wyoming, and Colorado. These hot spots have... where
 frequencies of...each about 20%, especially in the
 region...articularly between Colorado and Wyoming. In
 over...ore than 25% of the wind profiles, the...alyzed, N-
 LLJs can even be extracted. The N-LLJs over...ere
 identifiable. Along the Eastern US coast mainly extend... N-
 LLJs predominantly stretch from Maine to South Carolina,
 and their highest frequency can reach about ...with peak
 frequencies of approximately 15%-20%. The N-LLJs in...n
 eastern Quebec also occur... N-LLJs are most
 frequently...requent in winter (>25%). Over Hudson Bay,
 the ... exceeding 25%. The simulation can ...lso
 detect...etects the presence of N-LLJ from...n about 10% of
 ... [3]



310
 311 Figure 3. Seasonal occurrence frequency of N-LLJs. Frequency shown here is calculated by counting the number of
 312 occurrences of LLJs in each three-hourly time step and then dividing the total number of LLJs in each season by the number
 313 of time steps in that season.

314 **3.2.2 Southerly LLJs**

315 As to the patterns of S-LLJs in different seasons (see Figure 4), during winter, frequencies exceeding 10% are observed
 316 across a vast area spanning from south Texas and the western Gulf of Mexico to southern Iowa, depicted as a deep
 317 green area in Figure 4d. The greatest frequencies of S-LLJs (>20%) are found along the border between northeastern



删除了： climatology...atterns of S-LLJs in different seasons
 (see Figure 4), in...uring winter, in the broad region
 extending...requencies exceeding 10% are observed across a
 vast area spanning from the ...outh Texas-west...and the
 western Gulf of Mexico to southern Iowa, the frequencies of
 S-LLJs exceed 10%.
 ... [4]

446 Mexico and the United States. In addition, about 15% of the simulated wind profiles in south-central Texas are
447 identified as S-LLJs (red clusters). In the spring (March, April, and May), the frequency expands significantly in >10%
448 of areas, with clear S-LLJ distributions detected in Manitoba, Saskatchewan, and other parts of Canada. The highest
449 frequencies are still found in the Texas-Mexico area, where the magnitude of these frequencies increases to over 25%.
450 This region (colored purple) also extends northward to occupy most of Texas. In winter, S-LLJs with occurrence
451 frequencies of above 15% extend to near Colorado and Nebraska.

452 By summer, the area with frequencies greater than 10% no longer reaches to the central Canadian prairie provinces.
453 The S-LLJs over the western Gulf of Mexico become nearly indiscernible in modeled data, with frequencies
454 approaching 0%. Conversely, the area with frequencies exceeding 25% expands northward and is segmented into three
455 distinct parts: along the northeast Mexico-Texas border, west-central Texas, and the central US Great Plains (western
456 Oklahoma and southern Kansas). Regions where over 15% of wind profiles are identified as S-LLJs also spread from
457 Colorado to near South Dakota.

458 In the fall, the magnitude of the frequency of S-LLJs decreases dramatically in the central US Plains and Texas. The
459 frequency still maintains a level greater than 15% in most areas, but with a maximum frequency of only 20% and
460 sporadically located in southwest Texas. The frequencies greater than 10% again expand northward and eastward in
461 this season, reaching Manitoba and Ontario.

462 Additionally, several smaller-scale S-LLJs are evident on the seasonal S-LLJ distribution map. In spring, a narrow
463 region of S-LLJs with a frequency greater than 5% along the eastern side of the Appalachians extends from Georgia
464 through the western Atlantic to southern Nova Scotia. Near eastern Maryland over the Atlantic, the frequency of S-
465 LLJs can exceed 10%. This narrow frequency belt persists through summer with the same coverage, though the
466 frequency magnitude diminishes, and the presence of frequencies greater than 10% is no longer visible. In winter, a
467 region where S-LLJ frequency exceeds 5% stretches from southwest Oregon to the west coast of British Columbia.
468 Canada. However, by spring, S-LLJs with frequencies above 5% occur solely over the ocean west of British Columbia.
469 and in summer, S-LLJs are virtually undetectable in this region.

删除了: .

删除了: In...y summer, the area with frequencies greater than 10% no longer extends...eaches to the central Canadian prairie provinces and Tennessee.... The S-LLJs over the western Gulf of Mexico are also difficult to identify with ...ecome nearly indiscernible in modeled data, and their frequency is close to...ith frequencies approaching 0%. In contrast...onversely, the area with frequencies exceeding 25% extends...xpands northward in summer ...nd is roughly divided...egmented into three distinct parts distributed respectively in... along the northeast Mexico-Texas border, west-central Texas, and the central US Great Plains (western Oklahoma and southern Kansas). The regions...egions where more than...ver 15% of the ...ind profiles are identified as S-LLJ...LLJs also expand...pread from Colorado to near South Dakota. ...

... [5]

删除了: There are also...dditionally, several S-LLJs on a ...maller ...scale that can be seen...-LLJs are evident on the seasonal S-LLJ climatology...istribution map. In spring, a narrow region of S-LLJs with a frequency greater than 5% on...long the eastern side of the Appalachians extends from Georgia through the western Atlantic to southern Nova Scotia. Over the Atlantic near...ear eastern Maryland over the Atlantic, the frequency of the ...-LLJ...LLJs can exceed 10%. In summer, this...his narrow frequency belt still exists and has ...ersists through summer with the same coverage, but the magnitude of ...hough the frequency decreases and the frequency >...agnitude diminishes, and the presence of frequencies greater than 10% is no longer visible. In winter, a region where S-LLJ frequency is >...ceeds 5% extends...tretches from southwest Oregon to the west coast of British vf...olumbia, Canada. But in...owever, by spring, S-LLJs with frequencies >...bove 5% occur only...olely over the ocean west of British Columbia. As for the... and in summer, S-LLJs are almost...irtually undetectable in this region. ...

... [6]

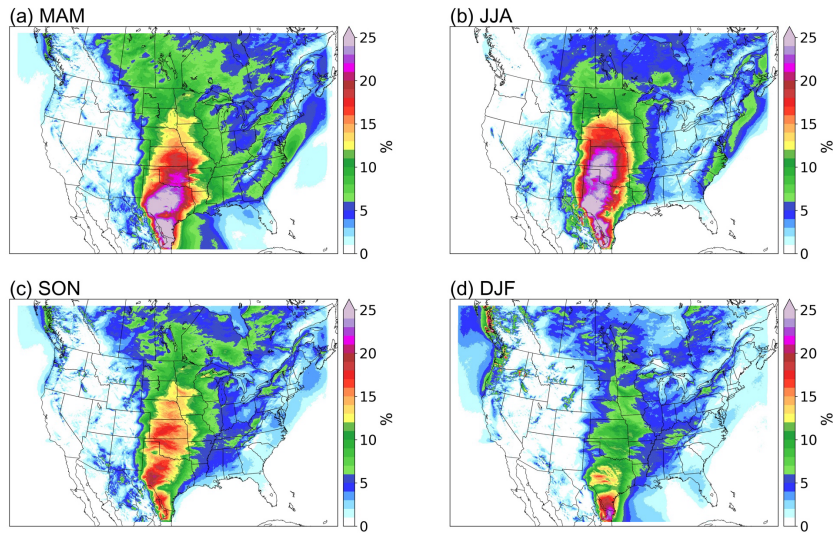


Figure 4. Seasonal frequency of S-LLJs.

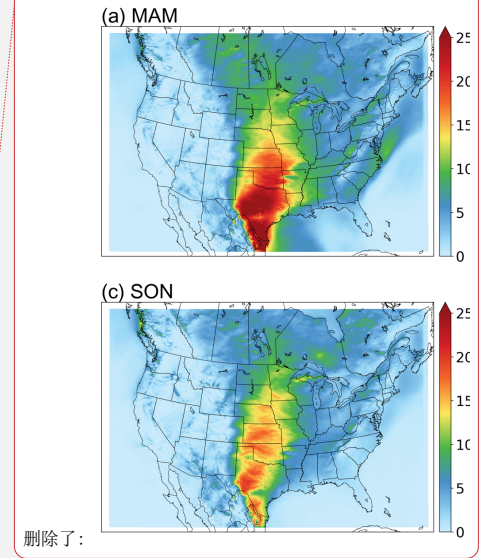
To summarize, for the LLJ systems that have been investigated by many researchers, the convection-permitting WRF model performs well in observing the Great Plains S-LLJ and California coastal N-LLJ during the summer. But as to the winter LLJs that lack attention, it is essential to compare and validate the occurrence and features revealed by WRF simulation. Therefore, the ERA5 reanalysis dataset is applied in this study for capturing the LLJs in winter using the same criterion. Appendix after the text shows the results of the comparison between ERA5 and WRF simulation.

3.3 Diurnal variations of LLJs

To show the diurnal features of the LLJs, we selected summer and winter as the representative seasons because S-LLJs and N-LLJs occur most frequently in these seasons, respectively. Below, the descriptions are divided into N-LLJs and S-LLJs.

3.3.1 Northerly LLJs

The California coastal N-LLJ is the most highlighted low-level jet system in this region in summer. As seen in Figure 5, it occurs throughout the day over the eastern Pacific Ocean from Oregon to the California coast. Figure 5 also shows that the California Coastal N-LLJ has diurnal characteristics: from 21 UTC (1 pm LST in California), the low-level

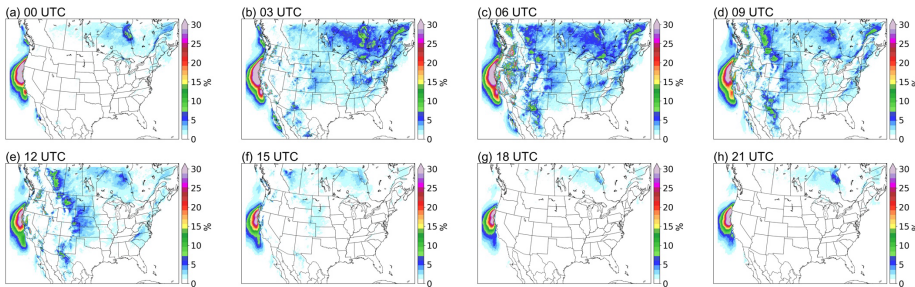


删除了:

删除了: .

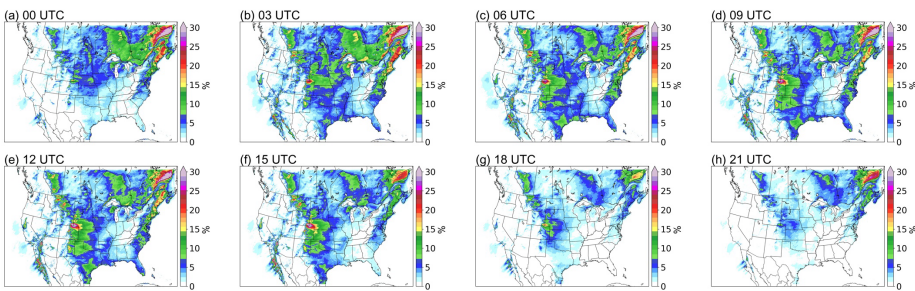
删除了: ,

590 jet begins to develop, with a N-LLJ frequency of >30%, expanding until it reaches its maximum at 03 UTC – 06 UTC.
 591 Then the high-frequency coverage of the California coastal LLJ gradually shrinks, reaching the minimum at 18 UTC
 592 and only existing off the northwest coast of California.



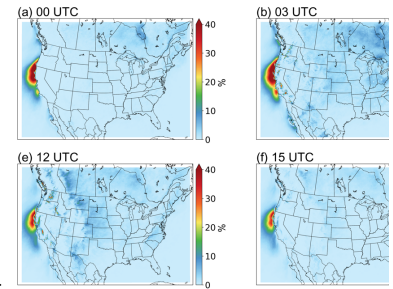
594 **Figure 5. Diurnal frequency of N-LLJs in the summer (JJA).**

595 In winter (Figure 6), three types of N-LLJs over the Hudson Bay Lowlands, the eastern slopes of the Quebec Labrador
 596 Plateau, and the Appalachians display similar diurnal fluctuations. All three N-LLJs reach their highest frequency at
 597 03 UTC (10 pm EST) and their lowest at 18 UTC (1 pm EST). The only difference among the three types is that the
 598 smallest frequency of the Quebec N-LLJ still endures at a level of greater than 15%, while the other two N-LLJs
 599 mostly have frequencies of about 5%. The smallest frequency (~5%) of N-LLJs occurs downstream of the Rocky
 600 Mountains (over Alberta, Montana, and Kansas) at 21 UTC. In the subsequent development stage, the changes in the
 601 sporadic hot spots distributed near the eastern boundary of the Rocky Mountains are more significant. As seen in
 602 Figure 6, frequency starts growing from 00 UTC and then peaks at 12 UTC, especially the wind maxima located in
 603 Colorado, Wyoming, and Kansas, where the highest frequency can be >25%.



604

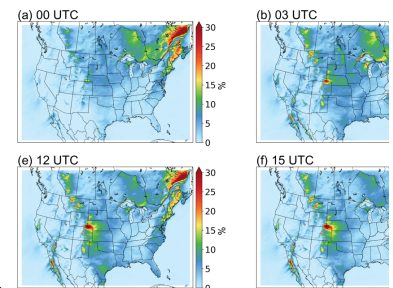
删除了: At the same time, the N-LLJ over the Hudson Bay Plain is also at its maximum frequency (>5%) from 03 UTC – 06 UTC, but it rarely occurs at other time steps.



删除了:

删除了: Plain

删除了: .

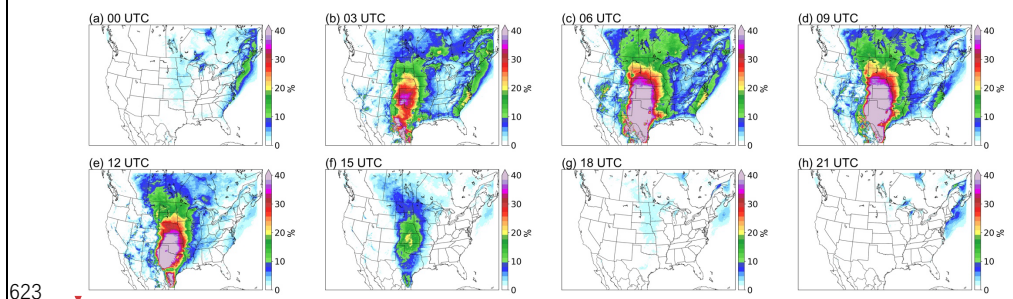


删除了:

612 **Figure 6. Diurnal frequency of N-LLJs in winter (DJF).**

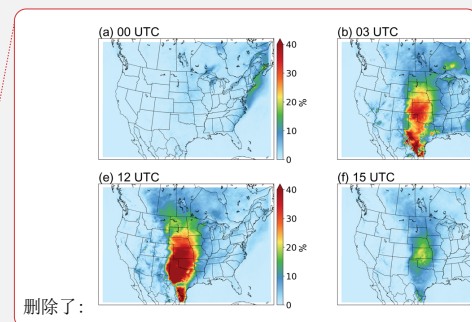
613 3.3.2 Southerly LLJs

614 In summer, the Great Plains S-LLJ occurs more frequently than in other seasons, and its diurnal variability is also the
615 strongest in this season (see Figure 7). At noon local time and in the afternoon (18 UTC – 00 UTC, **12-18 CST**), almost
616 no S-LLJs occur over the central US (frequency <5% or about 0%). In contrast, the Great Plains LLJ begins to develop
617 at 03 UTC, when a frequency of over 25% extends from Mexico to Kansas. It reaches maximum strength at midnight
618 (06 UTC – 09 UTC, **00 – 03 CST**), when the frequency reaches over 30% and the high-frequency coverage enlarges
619 to the Dakotas, the border of the eastern Rocky Mountains, and western Minnesota, Missouri, and Louisiana. Summer
620 S-LLJs are also active in southern Canada at night and in the early morning. In Saskatchewan, Manitoba, and central
621 Ontario (03 UTC – 12 UTC, as shown in Figure 7), S-LLJs are found with frequency >15%. In the eastern US and
622 Atlantic, S-LLJs occur most frequently at midnight (03 UTC – 06 UTC).

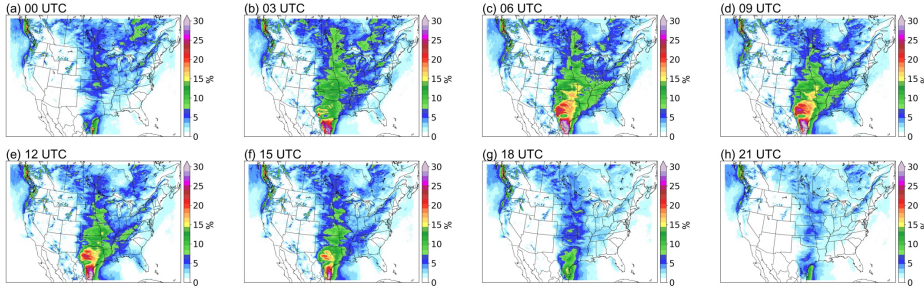


624 **Figure 7. Diurnal frequency of S-LLJs in summer (JJA).**

625 For the cold season (Figure 8), even though the Great Plains LLJ is the most inactive based on the description in
626 section 3.2, it still has a clear diurnal variation. Compared with the results in summer, the diurnal cycle of Great Plains
627 LLJ in winter is not that **pronounced**: It mainly occurs over the western Gulf of Mexico and southern Texas, with the
628 frequency in the afternoon (18 UTC – 21 UTC) declining to 5-10%. The S-LLJ develops from 03 UTC, gradually
629 generating two high-frequency (20%-25%) centers in mid- and southeastern Texas at 06 UTC – 12 UTC. As for the
630 S-LLJ near Vancouver Island, it is hard to see the diurnal variability: There is only a slight magnitude growth of
631 frequency from the afternoon (00 UTC) to the evening (06 UTC), and the coverage is almost the same.



删除了: significant



634

635

Figure 8. Diurnal frequency of S-LLJs in winter (DJF).

636

637

4 Formation and evolution mechanisms of various LLJs

638

Section 3's results illustrate the occurrence frequency of LLJs over North America, particularly their seasonal and

639

diurnal features. To explain the mechanisms, the inertial oscillation theory from Blackadar (1957) is used. Using this

640

theory, we start from the horizontal momentum equations and divide the actual horizontal wind u/v into two

641

components—geostrophic wind u_g/v_g and ageostrophic wind u_a/v_a :

642

$$\frac{d(u_g + u_a)}{dt} = -\frac{1}{\rho} \frac{\partial P}{\partial x} + f(v_g + v_a) \quad (1.1)$$

643

$$\frac{d(v_g + v_a)}{dt} = -\frac{1}{\rho} \frac{\partial P}{\partial y} - f(u_g + u_a) \quad (1.2)$$

644

645

In which ρ is air density, P is pressure, and f is the Coriolis parameter. Assuming the horizontal pressure gradient is

646

fixed, the geostrophic wind is a constant as well, which means $\frac{du_g}{dt} = \frac{dv_g}{dt} = 0$:

647

$$\frac{du_a}{dt} = -\frac{1}{\rho} \frac{\partial P}{\partial x} + f(v_g + v_a) \quad (2.2)$$

648

$$\frac{dv_a}{dt} = -\frac{1}{\rho} \frac{\partial P}{\partial y} - f(u_g + u_a) \quad (2.2)$$

649

650

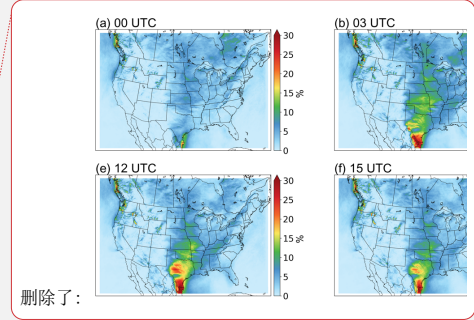
When the definition of geostrophic wind $u_g = -\frac{1}{\rho f} \frac{\partial P}{\partial y}$ and $v_g = \frac{1}{\rho f} \frac{\partial P}{\partial x}$ is combined, the equation (2) is:

651

$$\frac{du_a}{dt} = f v_a \quad (3.1)$$

652

$$\frac{dv_a}{dt} = -f u_a \quad (3.2)$$



删除了:

删除了: climatology

655

656 If $\frac{d}{dt}$ is taken to both sides of the equations (3), then we get $\frac{d^2 u_a}{dt^2} = -f^2 u_a$, and $\frac{d^2 v_a}{dt^2} = -f^2 v_a$, thereby:

657
$$u_a = c_1 \cos(ft) + c_2 \sin(ft) \quad (4.1)$$

658
$$v_a = c_2 \cos(ft) - c_1 \sin(ft) \quad (4.2)$$

659

660 Therefore, according to the equations (4), the ageostrophic wind should theoretically have a circle-pattern variation
661 and the vector must rotate clockwise with a period of $2\pi/f$ (Blackadar, 1957; Van de Wiel et al., 2010). Under the
662 condition of a constant geostrophic wind—when the ageostrophic vector rotates from the opposite to the same
663 direction of geostrophic wind—the wind transitions from subgeostrophic to supergeostrophic. This change occurs
664 because of decoupling with surface friction effects, then the wind gets unbalanced.

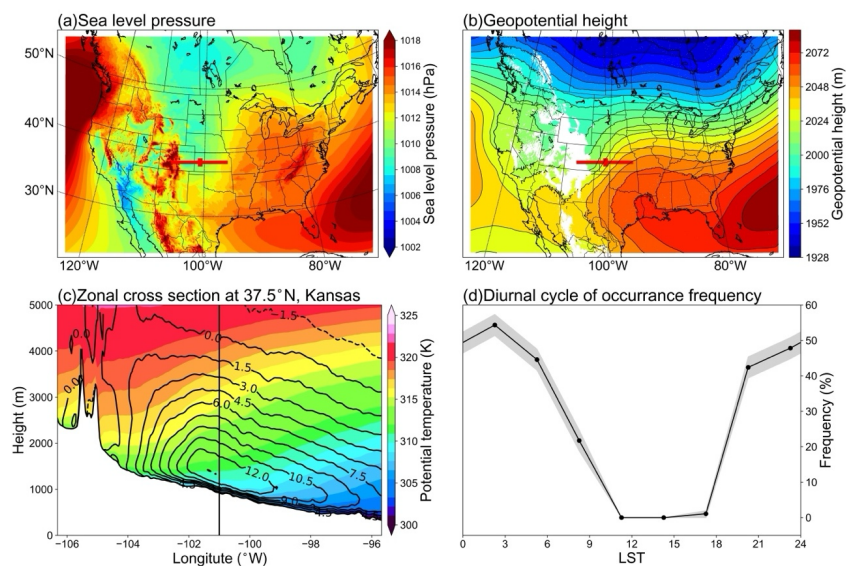
665 Other theories also help explain the formation of LLJs, such as the sloping-terrain thermodynamic mechanism (Holton,
666 1967) and background synoptic system forcing (Uccellini et al., 1987). To understand the characteristics of the LLJs
667 in this study, three typical cases are analyzed: Great Plains S-LLJ, Quebec N-LLJ, and California coastal N-LLJ. The
668 locations for extracting data are shown in Figure 1 (solid lines and stars a, b, c).

669 4.1 Great Plains S-LLJ

670 As Section 3's results show, (see Fig. 7), the Great Plains S-LLJ typically occurs in summer and more frequently at
671 night. To investigate its associated meteorological condition, this study extracts all the Great Plains S-LLJ cases occurs
672 at the jet core in JJA. The jet core is defined by where the mean meridional wind is the strongest on the cross-section,
673 and it locates at star A (shown in figure 1). The mean sea-level pressure and 800 hPa geopotential height are shown
674 in Figure 9a and 9b, respectively. The background large-scale circulations indicate that, at all the time points when
675 the Great Plains S-LLJ occurs, the range of the subtropical anticyclone extends east of the Great Plains at both ground
676 and low-level atmosphere. A high-pressure ridge is located near the gulf coast of Mexico and Texas (Figure 9b). Thus,
677 clearly, the zonal pressure/geopotential gradient in the central US guides the dominant southerly winds around this
678 region. The cross-section in Figure 9c illustrates a strong baroclinicity and shows that the isentropic line incline moves
679 from east to west, as is typical for the sloping-terrain heating effect (Holton, 1967). This effect generates an upslope
680 wind on the east side of the slope, and the airstream gradually turns northward due to the Coriolis force, creating the
681 southerly LLJs. On the other hand, as can be seen in the frequency cycle in Figure 9d, at noon local time (at the

删除了: ,

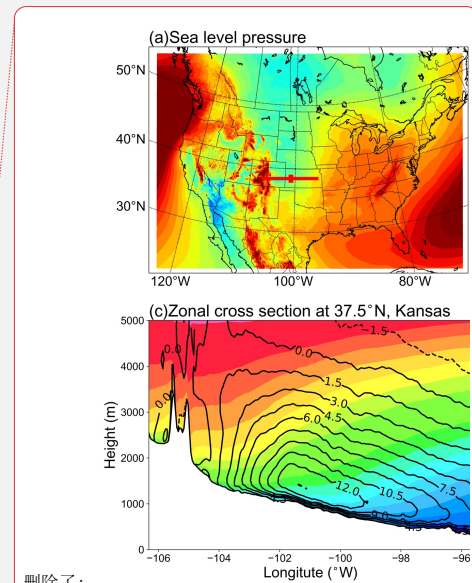
683 selected point-a in Figure 1), the frequency of the Great Plains LLJ is very low (close to 0%), rising to more than 40%
 684 after 18 LST even if the radiation is not at the day's peak.



685
 686 **Figure 9. Background circulations of the Great Plains S-LLJ in JJA: (a) sea-level pressure, (b) geopotential height of 800**
 687 **hPa, (c) cross section including meridional winds (lines) and potential temperature (shading), and (d) diurnal cycle of**
 688 **frequency, with the shaded 95% confidence intervals. The red lines and points in (a) and (b) show the position of cross-**
 689 **section and chosen jet core, the vertical line in (c) shows the zonal location of the chosen jet core.**

690 To explain the nighttime enhancement of S-LLJ, we analyzed the wind vectors using inertial oscillation theory. To
 691 show more significant diurnal variation, all the time points, including the LLJs that did not occur, were considered.
 692 Figure 10a is the hodograph of jet-core winds at point-a near the Great Plains, and their temporal mean is computed
 693 at 3-hourly intervals in summer. It is noted here that the “jet-core” means the position where LLJ occurs horizontally
 694 the most frequently on the cross-section. Compared with the mean actual wind (blue arrow), the deviation at each
 695 local time shows a clear clockwise rotation. The wind speed begins increasing after 17 LST. Nevertheless, the analysis
 696 for Figure 9 indicates the sloping heating effect, meaning that the geostrophic wind is not fixed.

697 Thus, to obtain the ageostrophic winds, we computed the geostrophic components by pressure gradient and subtracted
 698 them from the actual airflow. According to the aforementioned definition of geostrophic wind, u_g and v_g are



删除了:

删除了: .

701 calculated by the horizontal pressure gradient $\frac{\partial P}{\partial y}$ and $\frac{\partial P}{\partial x}$, respectively. By choosing four grids surrounding point-a, we

702 first interpolated the pressure value to the same level as the LLJ core height. Then, we adopted the central difference

703 equation $\frac{\Delta P}{\Delta x} = \frac{P_{i+1}-P_{i-1}}{x_{i+1}-x_{i-1}}$ or $\frac{\Delta P}{\Delta y} = \frac{P_{i+1}-P_{i-1}}{y_{i+1}-y_{i-1}}$ to obtain the pressure gradients at point-a, where i is the index of the grid

704 point at point-a.

705 Figures 10b and 10c display geostrophic wind vectors (blue arrows) and ageostrophic vectors (pink) at noon and

706 midnight. The southerly geostrophic flows are much stronger in the afternoon (10b) than at midnight. The ageostrophic

707 winds flow mostly in the opposite direction, limiting the actual wind speed. At night (10c), the geostrophic wind

708 direction rotates clockwise from that of the afternoon as the pressure gradient changes. Considering the relative

709 positions of blue and pink vectors at 23 LST and 01 LST, ageostrophic flow has rotated roughly 150 degrees to

710 enhance the geostrophic winds, thereby creating a super-geostrophic state. Although the inertial oscillation theory can

711 help explain some aspects of wind behavior, the real situation is more complex than initially thought. Figures 10b and

712 10c indicate that by 02 LST, the wind is almost entirely geostrophic with only negligible ageostrophic perturbations.

713 This suggests that the diurnal changes in the geostrophic wind and pressure gradient may provide a complicating

714 background that prevents the inertial oscillation theory from fully prevailing. While the inertial oscillation theory can

715 provide valuable insights, it should not be relied upon as the sole explanation for LLJs at the Great Plains. Instead, a

716 more comprehensive understanding of atmospheric dynamics is necessary to fully comprehend the behavior of the

717 wind, particularly when dealing with diurnally changing conditions. Figure 10d compares different meridional wind

718 components' amplitudes. The geostrophic wind contributes significantly to the southerly wind during the day, peaking

719 at 14 LST (blue bars). The northerly ageostrophic wind (red bars) is highest during the day, indicating the strongest

720 negative impact from friction. The meridional ageostrophic component decreases and eventually reverses at 23 LST,

721 showing a process from sub- to super-geostrophic status. In summary, the thermodynamic circulation near the slopes

722 of the Great Plains contributes to the strong southerly airflow, while the inertial oscillation plays a critical role in

723 forming the nocturnal southerly LLJ.

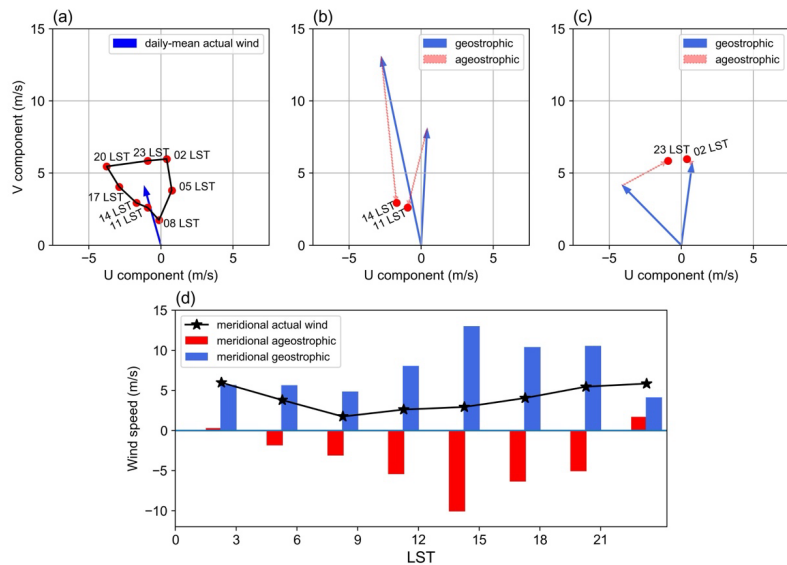
删除了: .

删除了: green

删除了: green

删除了: green

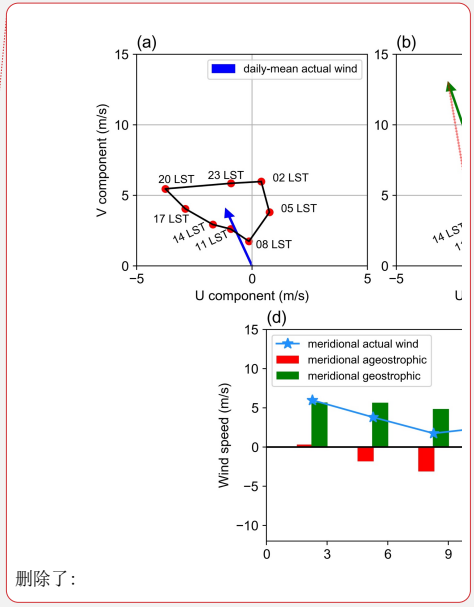
设置了格式: 字体: Times New Roman, 10 磅, 英语(英国)



729 **Figure 10. (a) Hodograph of jet-core winds for the Great Plains S-LLJ every 3 hours over the whole JJA (red dots – solid**
 730 **line) and the daily averaged actual wind velocity (blue vector); vectors of mean jet-core geostrophic winds (solid blue) and**
 731 **ageostrophic winds (dashed red) at (b) 11/14 LST and (c) 23/02 LST; (d) diurnal cycles of meridional components of actual**
 732 **(black line), geostrophic (blue bars), and ageostrophic winds (red bars).**

734 **4.2 Quebec N-LLJ**

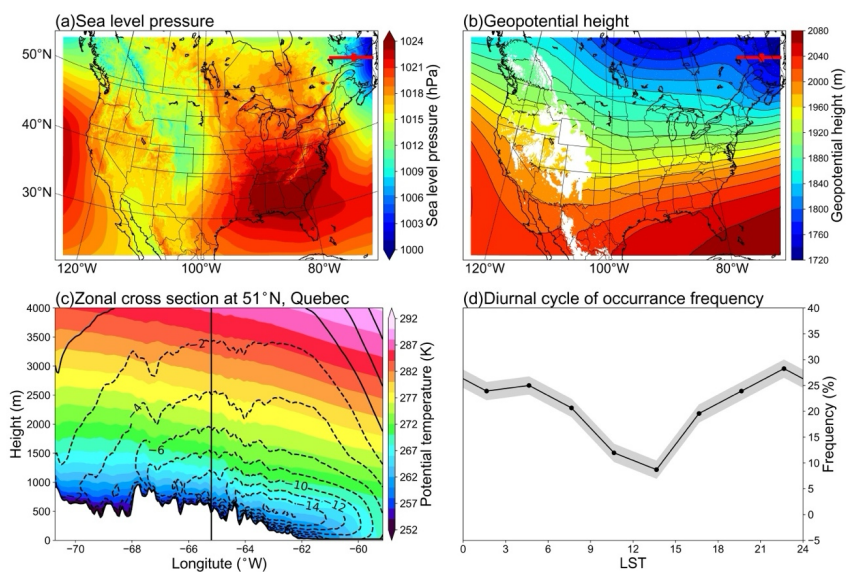
735 Similarly, for the Quebec N-LLJ that is typically observed in winter, we selected all the LLJ cases at point-b (see the
 736 position in Figure 1) in DJF to generate the background circulation pattern. The background large-scale circulations
 737 indicate that the northeastern coast of Canada lies to the west of a strong surface low-pressure system (Figure 11a),
 738 while in the lower troposphere, a ridge on the east side of Hudson Bay occupies the Labrador Plateau (Figure 11b).
 739 This combination brings the northerly momentum to the downstream eastern coast. In fact, the background circulation
 740 is consistent with the shallow baroclinic structure of Quebec N-LLJ in winter, that is, the thermal difference between
 741 relatively warm sea and cold land. The cross-section in Figure 11c shows the thermodynamic structure of this N-LLJ:
 742 A well-defined low-level jet core is located above land and close to the coastline (approximately 63°W). With a
 743 maximum wind speed of more than 16 m s⁻¹ and a height of about 400 m, the jet core is located above the mixed layer



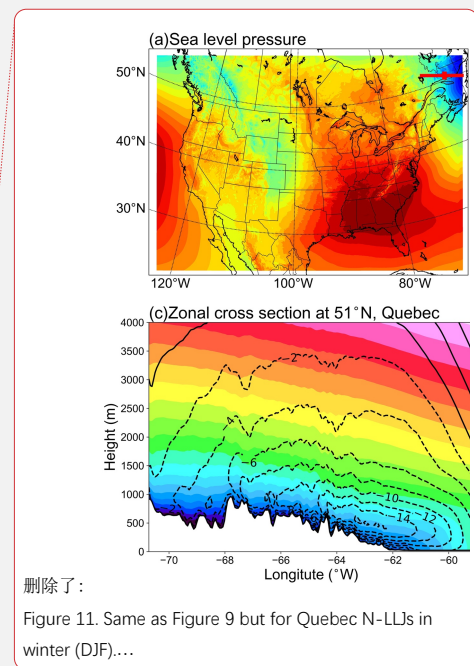
删除了:
 删除了: green
 删除了: blue
 删除了: green

748 under the warm air covering and on the land side. Notably, the steep isentropic lines slope towards the ocean and
 749 finally sink at the position of 60°W. The onshore isentropic lines are flat and dense above the LLJ core, which means
 750 the environment is quite stable. This is helpful to maintain the structure of the LLJ, when vertical motion is inhibited,
 751 and horizontal wind is enhanced. Compared with the sloped isentropic lines in the Great Plain S-LLJ case (Figure 9c),
 752 the stability over Great Plain is not as high as in this case, so this difference in stability helps explain the variation in
 753 wind speeds between these two cases.

754 In addition, the diurnal cycle of frequency (Figure 11d) shows that the diurnal signal and peak frequency of Quebec
 755 N-LLJ are much weaker than the Great Plains S-LLJ, becoming weakest at noon and peaking at midnight, which is
 756 consistent with the results reported in Section 3. This diurnal variation can be explained by the baroclinicity near this
 757 region: At night in winter, the land temperature drops faster than the ocean temperature due to radiative cooling,
 758 enhancing the land-sea contrast and thereby the thermal wind above. The gentle slope on the east of the Labrador
 759 Plateau could generate the slope heating effect in the daytime. In this way, the related temperature gradient from east
 760 to west offsets the land-sea thermal difference.



761
 762 **Figure 11. Background circulations of the Quebec N-LLJ in DJF: (a) sea-level pressure, (b) geopotential height of 800 hPa,**
 763 **(c) cross section including meridional winds (lines) and potential temperature (shading), and (d) diurnal cycle of frequency**

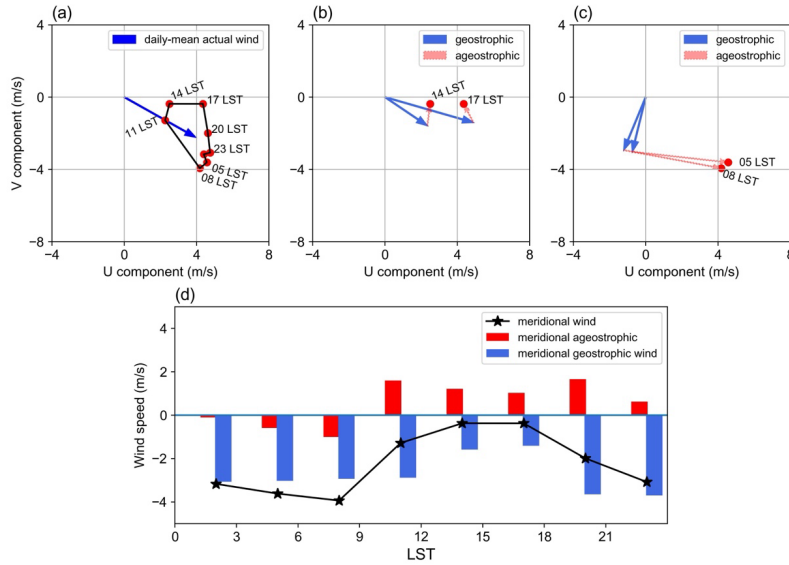


删除了:
 Figure 11. Same as Figure 9 but for Quebec N-LLJs in winter (DJF)....

767 with the shaded 95% confidence intervals. The red lines and points in (a) and (b) show the position of cross-section and
768 chosen jet core, the vertical line in (c) shows the zonal location of the chose jet core.

769 As for the impact of inertial oscillation on the Quebec N-LLJ, the hodograph of averaged 3-hourly winds extracted at
770 point-b (Figure 12a) also illustrates a clear clockwise rotation of wind deviations compared with the daily mean (blue
771 arrow). Figure 12b and 12c show that the geostrophic and ageostrophic wind vectors contribute to the diurnal cycle in
772 the afternoon and morning, respectively. Even though the direction of geostrophic wind changes significantly, the
773 relative angles between ageostrophic and geostrophic arrows indicate that the ageostrophic flow rotates clockwise.
774 The geostrophic wind is weakened by ageostrophic wind in the afternoon (Figure 12b), whereas the supergeostrophic
775 state is generated in the morning (Figure 12c).

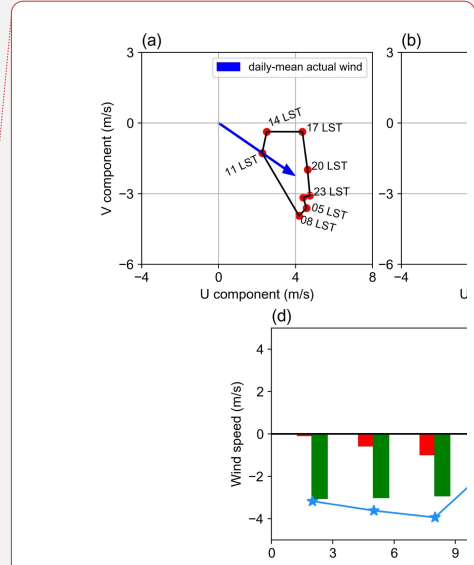
776 Focusing only on the meridional amplitudes validates this characteristic. In Figure 12d, the blue line that represents
777 the mean actual meridional wind has the same diurnal trend as the frequency variation in Figure 11d. The northerly
778 wind is weakest in the afternoon, peaking at night and in the early morning. Similarly, the variation of meridional
779 geostrophic flow has a consistent phase with the actual meridional wind, which is explained by the baroclinic structure
780 near the Quebec coast mentioned above. The meridional ageostrophic wind in this region also promotes the formation
781 of N-LLJ. The ageostrophic wind drags the geostrophic component in the afternoon, before reversing to a consistent
782 direction with the northerly geostrophic flow at night and in the morning. This trend is also the result of decreasing
783 friction after sunset. Therefore, the evolution of Quebec N-LLJ derives from both inertial oscillation and land-sea
784 thermal contrast in winter.



785
786 **Figure 12. (a) Hodograph of jet-core winds for the Quebec N-LLJ every 3 hours over the whole DJF (red dots – solid line)**
787 **and the daily averaged actual wind velocity (blue vector); vectors of mean jet-core geostrophic winds (solid blue) and**
788 **ageostrophic winds (dashed red) at (b) 14/17 LST and (c) 05/08 LST; (d) diurnal cycles of meridional components of actual**
789 **(black line), geostrophic (blue bars), and ageostrophic winds (red bars).**

790
791 **4.3 California coastal N-LLJ**

792 The California coastal N-LLJ is similar to the one in Quebec, but it occurs more often in summer afternoons or
793 evenings over the ocean. Figure 13a shows that a relatively strong high-pressure system is located on the east coast of
794 the Pacific Ocean, trending NE-SW, although half of the structure is beyond the boundary of the domain. On the 800
795 hPa isobaric surface in Figure 13b, there is also an anticyclone system in the same location, whose eastern contour is
796 roughly parallel to the coastline, guiding the airflow to the south. Therefore, this pair is also forced by the thermal
797 difference between land and sea, but contrary to the LLJ in Quebec, in summer, when the California LLJ occurs
798 frequently, it has the characteristics of the cool sea-hot land. Figure 13b also shows that the isobars near Cape
799 Mendocino are relatively strong, making the ridge of high pressure extend northeastward of the Cape. This extension
800 is generally believed to occur due to pressure perturbation caused when northerly winds converge at this position after



删除了:

790
791 **Figure 12. Same as Figure 10 but for Quebec N-LLJs in**
792 **winter (DJF).**

804 being obstructed (Rahn and Parish, 2007). Regarding the cross-section structure shown in Figure 13c, the jet core is
 805 located at steep isentropic lines above the ocean at a height of 500 m. On the coast of California, the LLJ is close to
 806 the mountains. The maximum central wind speed of California coastal LLJ exceeds 20 m s⁻¹, whereas Quebec N-
 807 LLJ's max core wind is only about 14 m s⁻¹. Based on baroclinicity, the isentropic lines slope towards the continent
 808 and finally sink near the coastline.

809 The core wind speed in California's coastal LLJ is higher than that of Quebec's LLJ because the land-sea contrast is
 810 more significant in summer than in winter and the formed sea breeze front generates flow convergence under the
 811 blockage caused by the west coast mountains. On the other hand, the atmosphere over the sea is more stable because
 812 the isentropic lines are flatter and denser than Quebec's case, which also favors the development of LLJ. In contrast,
 813 the east coast of Quebec is relatively gentle, which may account for its lower wind speed. California's LLJ occurs
 814 frequently at each time step, and its diurnal signal is weaker compared, for example, to the signal in the Great Plain
 815 S-LLJ. As well, the California signal stays at frequency of over 35%. California's LLJ occurs most frequently at
 816 around 18 LST and starts to decline after sunset, which is generally consistent with the coastal baroclinicity.

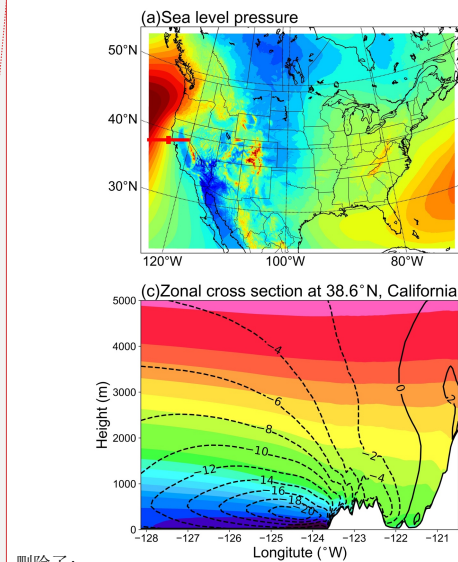
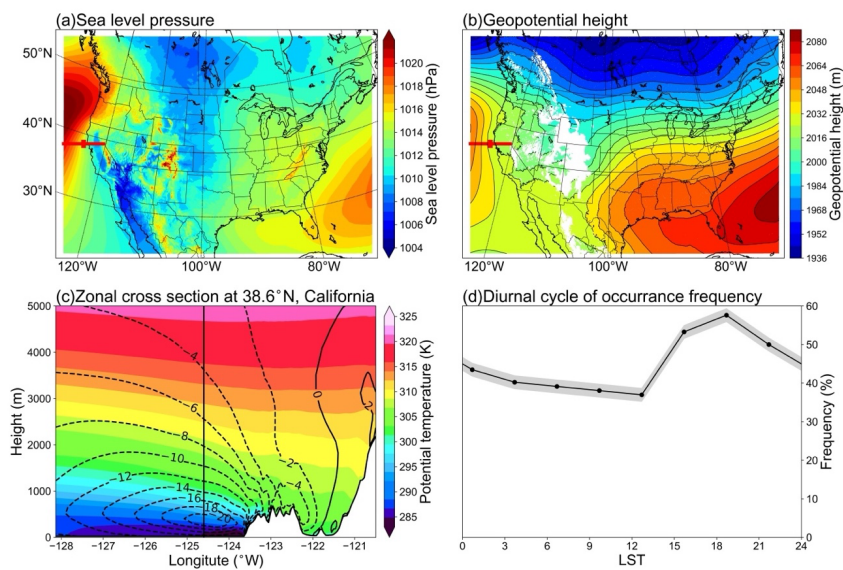
删除了: Compared with the Quebec LLJ, California's

删除了: may be

删除了: Because California's

删除了: (13d), the

删除了: weak



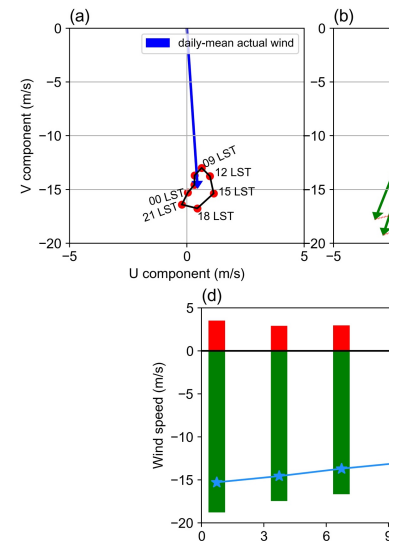
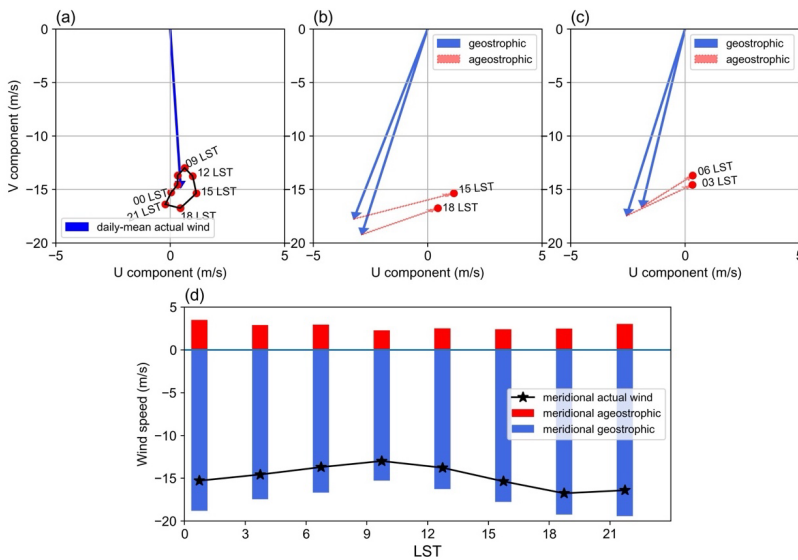
删除了:

Figure 13. Same as Figure 9 but for California Coastal S-LLJ in summer (JJA).

817
 818 **Figure 13. Background circulations of the California coastal N-LLJ in JJA: (a) sea-level pressure, (b) geopotential height**
 819 **of 800 hPa, (c) cross section including meridional winds (lines) and potential temperature (shading), and (d) diurnal cycle**

828 of frequency with the shaded 95% confidence intervals. The red lines and points in (a) and (b) show the position of cross-
 829 section and chosen jet core, the vertical line in (c) shows the zonal location of the chosen jet core.

830
 831 The wind deviations for California's N-LLJ shown in the hodograph (Figure 14a) still have a clockwise rotation in 24
 832 hours. However, compared with the magnitude of the daily mean jet-core wind, this diurnal cycle is not quite as
 833 obvious as the cycle for Quebec and Great Plain LLJs, but it is similar to the frequency cycle shown in Figure 13d. In
 834 comparison between geostrophic and ageostrophic winds (Figure. 14b and 14c), during the afternoon (15 and 18 LST),
 835 the amplitude of geostrophic wind is the largest, and the ageostrophic flow diminishes the geostrophic wind. However,
 836 in the morning 12 hours later, the relative angle between ageostrophic and geostrophic vectors does not change,
 837 meaning that the ageostrophic wind is still weakening the geostrophic wind and that there is no rotation of the
 838 ageostrophic wind, as Blackadar inertial oscillation theory describes. Figure 14d helps to explain the change in
 839 meridional winds. Looking at the magnitudes of ageostrophic winds, one can see that all are weak and southerly and
 840 that they do not exhibit a significant diurnal signal. Furthermore, the change of geostrophic wind is highly consistent
 841 with the trend of the actual meridional wind. Thus, the N-LLJ in California can be considered mostly as geostrophic
 842 and the diurnal variation as being related to the change in geostrophic winds.



删除了:

Figure 14. Same as Figure 10 but for California Coastal S-LLJ in summer (JJA).

847 Figure 14. (a) Hodograph of jet-core winds for the California coastal N-LLJ every 3 hours over the whole JJA (red dots –
848 solid line) and the daily averaged actual wind velocity (blue vector); vectors of mean jet-core geostrophic winds (solid blue
849 and ageostrophic winds (dashed red) at (b) 15/18 LST and (c) 03/06 LST; (d) diurnal cycles of meridional components of
850 actual (black line), geostrophic (blue bars), and ageostrophic winds (red bars).

851

852 5 Discussion and conclusion

853 This study applied a convection-permitting WRF model to conduct the analysis of LLJs in North America. The
854 previous research for LLJs mainly focused on observation data, which have no fine coverage in temporal or spatial
855 resolution. The studies using in-situ observations may ignore some important features. Despite their better coverage,
856 reanalysis datasets usually have a coarse spatial resolution, and can introduce large inaccuracies in the identification
857 of LLJs. In addition, the application of general numerical modeling cannot avoid the uncertainty caused by
858 parameterizing small-scale physical processes. In contrast, high-resolution convection-permitting climate simulations
859 can provide relatively more comprehensive descriptions of LLJs, especially for areas with complex geographic
860 conditions or regions that lack soundings. Previous studies using high-resolution models conducted case analyses only
861 of LLJs in a specific region (Aird et al., 2022). By expanding the target domain to the whole of North America and
862 revealing the climatological characteristics of LLJs in different regions and scales, this paper provides an accurate
863 reference for future research on LLJ-related processes in North America.

864 The convection-permitting WRF model is able to recapture some LLJs that have been previously studied, such as the
865 Great Plain S-LLJ and the California coastal N-LLJ in the eastern Pacific Ocean and has obtained relatively consistent
866 results. The results indicate that the S-LLJ in the central US Plain is the most frequent and active in warm seasons and
867 that three critical high-frequency centers occur in summer: the northeast Mexico-Texas border, west-central Texas,
868 and western Oklahoma to southern Kansas. This last result is consistent with the climatology generated by Doubler et
869 al. (2015) using the NARR reanalysis data, but the patterns here are more representative of the topographic features
870 in central and southern Texas. In addition, compared with the 40-year rawinsonde climatology in the central US by
871 Walters et al. (2008), our study reveals that the S-LLJ frequency range of these three centers in the central US in
872 summer is 25%-30%, which is slightly lower than the 35% reported in the 2008 study. However, given the
873 underestimated frequencies of 15%-20% in NARR climatology, there is an advantage of using high-resolution
874 simulations in the vertical direction. Even though the simulation period does not match the time range of the literature
875 exactly, the characteristics transcend specific time frames still offer a reference.

删除了: generate

删除了: climatology

删除了: especially in the vertical direction,

删除了: reliable and accurate

880 ~~The convection-permitting simulation can also capture LLJs that were poorly detected previously using coarser~~
881 ~~resolution models and observational datasets.~~ The winter N-LLJs over the eastern Rocky Mountains described in this
882 paper are generally distributed over the central US from the Dakotas to Oklahoma with a low frequency (>10%) and
883 over several sporadic small areas with a high frequency (>20%) along the boundary of the Rockies. The main
884 seasonal/diurnal variations identified in this study agree with those seen using rawinsonde data (Walters et al., 2008)
885 and NARR reanalysis (Douber et al., 2015). But the frequency of the LLJ occurrence over Nebraska-Kansas was
886 underestimated in both convection-permitting simulations (~10%) and NARR (~7%), while high-frequency hot spots
887 from Alberta to Colorado were not detected in either of the above-mentioned studies, probably because measurements
888 are lacking in these regions. The high-resolution simulation also detected LLJs on which researchers have hardly
889 focused: N-LLJs near the eastern Quebec coast and in the Appalachians Mountains, as well as an S-LLJ over the
890 British Columbia coast. In the work of Douber et al. (2015), these LLJs were shown in the climatology patterns, but
891 the 4-km WRF simulation offered more detailed descriptions of their locations. For example, this study found that the
892 Appalachian N-LLJ extends from Georgia to the northwestern Atlantic, especially on summer nights (03 UTC – 06
893 UTC), while NARR only captured LLJ occurrences over the middle coast of the Atlantic. The maximum frequency
894 (7-10%) detected in the NARR study is also less than what is illustrated here. As for the Quebec N-LLJ, the 4-km
895 WRF revealed that it mostly occurs onshore near the coast with a frequency of over 25% in winter, but NARR only
896 provided a coarse occurrence distribution over northeastern Canada. ▼

897 Based on the inertial oscillation theory (Blackadar, 1957) and the baroclinic theory near complex terrain (Holton,
898 1967), this paper also analyzed the background and formation mechanisms of three LLJs: the Great Plain S-LLJ,
899 Quebec N-LLJ, and California coastal N-LLJ. Generally, all these LLJs are impacted by the thermodynamic
900 circulations generated near their topography. The Great Plain S-LLJ is affected by slope heating, and the LLJs over
901 Quebec and California are associated with the sea-land contrast. When the geostrophic and ageostrophic components
902 of the LLJs are compared, results show that the inertial oscillation better explains the night enhancement of the Great
903 Plains S-LLJ and that the diurnal feature of the Quebec N-LLJ is influenced by the combination of the Holton and
904 Blackadar theories. As for the California coastal N-LLJ, no supergeostrophic state is found, making coastal
905 baroclinicity variation a dominant factor for this LLJ's evolution the geostrophic wind changes.

删除了: Convection

删除了: simulations

删除了: the

删除了: barely

带格式的: 正文, 段落间距段后: 0.5 行, 行距: 1.5 倍行距

删除了: ↵

To investigate the significance of LLJs in different regions, Figures 15 and 16 demonstrate the impact of the Great Plains S-LLJ and Quebec N-LLJ, respectively, on downstream extreme precipitation during their active seasons. Figure 15a illustrates the 90th percentile of summer precipitation in the central United States, indicating that 90% of the precipitation in most areas falls within the range of 1.0-2.0 mm/hour. However, Figure 15b shows the ratio of strong events related to LLJs (counted if the precipitation is > 90th percentile when a LLJ occurs) to all strong events, with the red outline on the map indicating the approximate location of the low-level jet stream. It is evident that in the lower reaches of the S-LLJ in the Great Plain, particularly in the north-central United States, nearly 50% of the heavy precipitation events are associated with the flourishing low-level jet stream. Furthermore, Figure 15c displays the average precipitation of all LLJ-related strong events. Compared with Figure 15a, some areas of Nebraska and Minnesota experience rainfall of up to 6mm/hour. These findings highlight the significant role played by LLJ in modulating summer precipitation. Similarly, for the Quebec N-LLJ in winter (Fig. 16), it contributes more than 25% of the strong events of precipitation in the Gulf of St. Lawrence during winter (Fig. 16b). Figure 16c further reveals that, in comparison to the 90th percentile rainfall, the extreme precipitation from Quebec to Maine is approximately 1mm/hr higher. Particularly during the cold season when a substantial portion of precipitation is snow, the N-LLJs can also be seen as the factors of snowstorms in this region. In summary, research on the importance of LLJs includes not only the field of extreme precipitation, but also local wind energy production, air pollution dispersion, wildfires, etc.

(Jain & Flannigan 2021, Lin et al. 2022, Weide Luiz & ... [7])

设置了格式: 字体: Times New Roman, 10 磅, 英语(英国)

983 ~~This research adds to the existing knowledge of characteristics of the low-level wind maxima in North America, thus~~
984 ~~helping researchers obtain more reliable references about LLJs in this domain. Meanwhile, with the high-resolution~~
985 ~~features, it can provide more robust explanations for other interdisciplinary fields. The research also advances~~
986 ~~knowledge about the formation of three dominant LLJs. Although the 13-year simulation is likely too short to provide~~
987 ~~an ideal long-term climatic analysis, it is a less expensive option for finer numerical modelling in large domains.~~
988 ~~Additionally, we acknowledge certain limitations in the convection-permitting WRF simulation. While the vertical~~
989 ~~resolution in the boundary layer of this simulation is enhanced compared to other RCMs or reanalysis datasets, it~~
990 ~~remains inferior to the observation density of radiosonde soundings. Consequently, the underestimation of LLJ events~~
991 ~~in this paper is expected, as noted in previous comparative analyses. Furthermore, numerical models inherently possess~~
992 ~~biases and uncertainties. Although employing the convection-permitting scale mitigates some of these uncertainties,~~
993 ~~it is important to recognize these limitations in referring to the results. But it is also believed that with the advancement~~
994 ~~of technology, there will be longer and more accurate~~ high-resolution simulations in the future. Future work will
995 address the features and formation mechanisms of the small-scale low-level wind maxima that have yet to be
996 investigated.

删除了： The LLJs climatology introduced in this

删除了： modeling in large domains. But it is also believed that with the advancement of technology, there will be longer

1000 **Acknowledgments**

1001 All authors thank the support of the Global Water Futures Program by the Canada First Research Excellence and the
1002 NSERC Discovery Grant.

1003
1004 **Data Availability Statement**

1005 The WRF simulation over CONUS can be accessed at Research Data Archive of NCAR
1006 <https://rda.ucar.edu/datasets/ds612.0/>.

1007
1008 **Author contribution**

1009 Xiao Ma: Conceptualization; data curation; formal analysis; investigation; methodology; visualization; writing-
1010 original draft.

1011 Yanping Li: Conceptualization; funding acquisition; investigation; methodology; project administration; supervision;
1012 validation; writing-review and editing.

1013 Zhenhua Li: Data curation; methodology; validation; visualization; writing-review and editing.

1014 Fei Huo: Data curation; methodology; validation; visualization; writing-review and editing.

1015
1016 **Competing interests**

1017 All authors disclosed no relevant relationships.

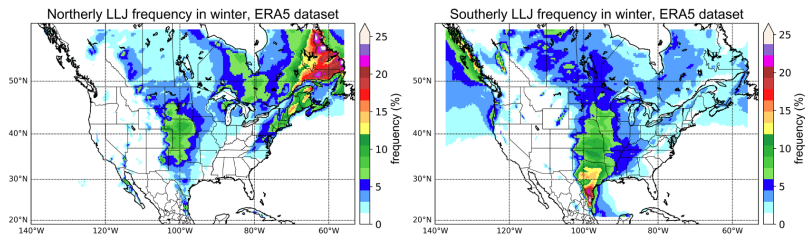
1018

1019 **Appendix**

1020 **Winter LLJs captured by ERA5 Dataset**

1021 The convection-permitting WRF simulation exhibited excellent performance in investigating well-known LLJ systems,
1022 such as the California coastal N-LLJ and the Great Plains S-LLJ. Moreover, this appendix validates WRF-simulated
1023 significant winter jet systems over North America using the ERA5 reanalysis dataset. ERA5 is a global atmospheric
1024 reanalysis dataset produced by the European Centre for Medium-Range Weather Forecasts (ECMWF). It provides
1025 hourly data on a horizontal grid space of approximately 31 km, and the time range covers from 1979 till the present.
1026 ERA5 data is widely used in climate research, weather forecasting, and various applications that require high-quality
1027 atmospheric data.

1028 The validation period is the same as the WRF simulation (2000-2013). From the Figure A1 below, it is evident that
1029 during winter, a greater number of significant N-LLJ systems in the North American continent are mostly concentrated
1030 in eastern Canada. In most parts of Newfoundland and southeastern Quebec, the occurrence frequency of N-LLJs
1031 exceeds 15%, and the maximum can even surpass 25%. However, in the WRF simulation (Figure 3d), the model can
1032 only capture N-LLJs on the north bank of the St. Lawrence River due to the northern boundary of the study domain
1033 overlapping with the Quebec border. In comparison, the WRF-simulated frequency of N-LLJs in southeastern Quebec
1034 essentially exceeds 25%, overestimated by about 5% compared to the ERA5 reanalysis. Additionally, it is worth noting
1035 that the N-LLJs along the downstream of Rockies are also identified in the ERA5 dataset. The areas where the
1036 frequency exceeds 5% are mainly distributed from Alberta to northern Texas, consistent with the findings in Section
1037 3.2.1. Moreover, the high-value center (>10%) is located in central Kansas. In terms of the differences between the
1038 two datasets, the results of the WRF simulation match more geographical features and reveal scattered high-value
1039 spots (>15%) in some regions with special terrains (see Figure 3d). Furthermore, the winter Great Plains S-LLJs in
1040 ERA5 reanalysis exhibit similar features, with frequencies ranging from around 15% to 20% in southern Texas. In
1041 summary, the WRF model can accurately capture the features of winter LLJ systems, which are validated by the ERA5
1042 reanalysis dataset over northern America. Even though the frequency of LLJs occurrence is overestimated, the
1043 convection-permitting WRF simulation can provide detailed descriptions of LLJs near complex terrains.



1044

1045 **Figure A1. Winter occurrence frequency of N-LLJs (left) and S-LLJs (right).**

1046

1047

1048

1049 **Data Availability Statement**

1050 The ERA5 dataset is available on the Copernicus Climate Change Service Information website.

1051 <https://cds.climate.copernicus.eu/#!/home>

1052

1053

-
- 1054 **References**
- 1055 Aird, J. A., Barthelmie, R. J., Shepherd, T. J. and Pryor, S. C.: Occurrence of Low-Level Jets over the Eastern U.S.
1056 Coastal Zone at Heights Relevant to Wind Energy, *Energies*, 15(2), 445, doi:10.3390/en15020445, 2022.
- 1057 Blackadar, A. K.: Boundary Layer Wind Maxima and Their Significance for the Growth of Nocturnal Inversions,
1058 *Bulletin of the American Meteorological Society*, 38(5), 283–290, doi:10.1175/1520-0477-38.5.283, 1957.
- 1059 Bonner, W. D.: CLIMATOLOGY OF THE LOW LEVEL JET, *Monthly Weather Review*, 96(12), 833–850,
1060 doi:10.1175/1520-0493(1968)096<0833:cotllj>2.0.co;2, 1968.
- 1061 Chen, G. T.-J., Wang, C.-C. and Lin, D. T.-W.: Characteristics of Low-Level Jets over Northern Taiwan in Mei-Yu
1062 Season and Their Relationship to Heavy Rain Events, *Monthly Weather Review*, 133(1), 20–43, doi:10.1175/mwr-
1063 2813.1, 2005.
- 1064 Doubler, D. L., Winkler, J. A., Bian, X., Walters, C. K. and Zhong, S.: An NARR-Derived Climatology of Southerly
1065 and Northerly Low-Level Jets over North America and Coastal Environs, *Journal of Applied Meteorology and*
1066 *Climatology*, 54(7), 1596–1619, doi:10.1175/jamc-d-14-0311.1, 2015.
- 1067 Du, Y. and Chen, G.: Heavy Rainfall Associated with Double Low-Level Jets over Southern China. Part II: Convection
1068 Initiation, *Monthly Weather Review*, 147(2), 543–565, doi:10.1175/mwr-d-18-0102.1, 2019.
- 1069 Frisch, A. S., Orr, B. W. and Martner, B. E.: Doppler Radar Observations of the Development of a Boundary-Layer
1070 Nocturnal Jet, *Monthly Weather Review*, 120(1), 3–16, doi:10.1175/1520-
1071 0493(1992)120<0003:drootd>2.0.co;2, 1992.
- 1072 Fu, P., Zhu, K., Zhao, K., Zhou, B. and Xue, M.: Role of the nocturnal low-level jet in the formation of the morning
1073 precipitation peak over the Dabie Mountains, *Advances in Atmospheric Sciences*, 36(1), 15–28, doi:10.1007/s00376-
1074 018-8095-5, 2018.
- 1075 Gadde, S. N. and Stevens, R. J. A. M.: Effect of low-level jet height on wind farm performance, *Journal of Renewable*
1076 *and Sustainable Energy*, 13(1), 013305, doi:10.1063/5.0026232, 2021.

1077 Hodges, D. and Pu, Z.: Characteristics and Variations of Low-Level Jets and Environmental Factors Associated with
1078 Summer Precipitation Extremes over the Great Plains, *Journal of Climate*, 32(16), 5123–5144, doi:10.1175/jcli-d-18-
1079 0553.1, 2019.

1080 [Hoffmann, L. and Spang, R.: An assessment of tropopause characteristics of the ERA5 and era-interim meteorological](#)
1081 [reanalyses, *Atmospheric Chemistry and Physics*, 22\(6\), 4019–4046, doi:10.5194/acp-22-4019-2022, 2022.](#)

1082 Holton, J. R.: The diurnal boundary layer wind oscillation above sloping terrain, *Tellus*, 19(2), 199–205,
1083 doi:10.1111/j.2153-3490.1967.tb01473.x, 1967.

1084 Hong, S.-Y., Noh, Y. and Dudhia, J.: A New Vertical Diffusion Package with an Explicit Treatment of Entrainment
1085 Processes, *Monthly Weather Review*, 134(9), 2318–2341, doi:10.1175/mwr3199.1, 2006.

1086 Hu, X.-M., Klein, P. M., Xue, M., Lundquist, J. K., Zhang, F. and Qi, Y.: Impact of Low-Level Jets on the Nocturnal
1087 Urban Heat Island Intensity in Oklahoma City, *Journal of Applied Meteorology and Climatology*, 52(8), 1779–1802,
1088 doi:10.1175/jamc-d-12-0256.1, 2013.

1089 Iacono, M. J., Delamere, J. S., Mlawer, E. J., Shephard, M. W., Clough, S. A. and Collins, W. D.: Radiative forcing
1090 by long-lived greenhouse gases: Calculations with the AER radiative transfer models, *Journal of Geophysical*
1091 *Research*, 113(D13), doi:10.1029/2008jd009944, 2008.

1092 Jain, P. and Flannigan, M.: The relationship between the Polar Jet Stream and extreme wildfire events in North
1093 America, *Journal of Climate*, 1–59, doi:10.1175/jcli-d-20-0863.1, 2021.

1094 Jiménez-Sánchez, G., Markowski, P. M., Jewtoukoff, V., Young, G. S. and Stensrud, D. J.: The Orinoco Low-Level
1095 Jet: An Investigation of Its Characteristics and Evolution Using the WRF Model, *Journal of Geophysical Research:*
1096 *Atmospheres*, 124(20), 10696–10711, doi:10.1029/2019jd030934, 2019.

1097 Kurkute, S., Li, Z., Li, Y. and Huo, F.: Assessment and projection of the water budget over Western Canada using
1098 convection-permitting weather research and forecasting simulations, *Hydrology and Earth System Sciences*, 24(7),
1099 3677–3697, doi:10.5194/hess-24-3677-2020, 2020.

1100 Li, Y., Li, Z., Zhang, Z., Chen, L., Kurkute, S., Scaff, L. and Pan, X.: High-resolution regional climate modeling and
1101 projection over Western Canada using a weather research forecasting model with a pseudo-global warming approach,
1102 *Hydrology and Earth System Sciences*, 23(11), 4635–4659, doi:10.5194/hess-23-4635-2019, 2019.

1103 Lin, Y., Wang, C., Yan, J., Li, J. and He, S.: Observation and simulation of low-level jet impacts on 3D urban heat
1104 islands in Beijing: A case study, *Journal of the Atmospheric Sciences*, 79(8), 2059–2073, doi:10.1175/jas-d-21-0245.1,
1105 2022.

1106 Liu, C., Ikeda, K., Rasmussen, R., Barlage, M., Newman, A. J., Prein, A. F., Chen, F., Chen, L., Clark, M., Dai, A.,
1107 Dudhia, J., Eidhammer, T., Gochis, D., Gutmann, E., Kurkute, S., Li, Y., Thompson, G. and Yates, D.: Continental-
1108 scale convection-permitting modeling of the current and future climate of North America, *Climate Dynamics*, 49(1–
1109 2), 71–95, doi:10.1007/s00382-016-3327-9, 2016.

1110 Ma, X., Li, Y. and Li, Z.: The projection of Canadian wind energy potential in future scenarios using a convection-
1111 permitting regional climate model, *Energy Reports*, 8, 7176–7187, doi:10.1016/j.egyr.2022.05.122, 2022.

1112 Miao, Y., Guo, J., Liu, S., Wei, W., Zhang, G., Lin, Y., Zhai, P., Zhai, P., Lin, Y., Zhang, G., Wei, W., Liu, S., Guo,
1113 J. and Miao, Y.: The Climatology of Low-Level Jet in Beijing and Guangzhou, China, *Journal of Geophysical*
1114 *Research: Atmosphere*, 123(5), 2816–2830, doi:10.1002/2017jd027321, 2018.

1115 Mitchell, M. J., Arritt, R. W. and Labas, K.: A Climatology of the Warm Season Great Plains Low-Level Jet Using
1116 Wind Profiler Observations, *Weather and Forecasting*, 10(3), 576–591, doi:10.1175/1520-
1117 0434(1995)010<0576:acotws>2.0.co;2, 1995.

1118 Montini, T. L., Jones, C. and Carvalho, L. M. V.: The South American Low-Level Jet: A New Climatology, Variability,
1119 and Changes, *Journal of Geophysical Research: Atmospheres*, 124(3), 1200–1218, doi:10.1029/2018jd029634, 2019.

1120 Munday, C., Washington, R. and Hart, N.: African Low-Level Jets and Their Importance for Water Vapor Transport
1121 and Rainfall, *Geophysical Research Letters*, 48(1), doi:10.1029/2020gl090999, 2021.

1122 Niu, G.-Y., Yang, Z.-L., Mitchell, K. E., Chen, F., Ek, M. B., Barlage, M., Kumar, A., Manning, K., Niyogi, D.,
1123 Rosero, E., Tewari, M. and Xia, Y.: The community Noah land surface model with multiparameterization options
1124 (Noah-MP): 1. Model description and evaluation with local-scale measurements, *Journal of Geophysical Research*,
1125 116(D12), doi:10.1029/2010jd015139, 2011.

1126 Parish, T. R.: Forcing of the Summertime Low-Level Jet along the California Coast, *Journal of Applied Meteorology*,
1127 39(12), 2421–2433, doi:10.1175/1520-0450(2000)039<2421:fotsll>2.0.co;2, 2000.

1128 Rahn, D. A. and Parish, T. R.: Diagnosis of the Forcing and Structure of the Coastal Jet near Cape Mendocino Using
1129 In Situ Observations and Numerical Simulations, *Journal of Applied Meteorology and Climatology*, 46(9), 1455–1468,
1130 doi:10.1175/jam2546.1, 2007.

1131 Rife, D. L., Pinto, J. O., Monaghan, A. J., Davis, C. A. and Hannan, J. R.: Global Distribution and Characteristics of
1132 Diurnally Varying Low-Level Jets, *Journal of Climate*, 23(19), 5041–5064, doi:10.1175/2010jcli3514.1, 2010.

1133 Saulo, C., Ruiz, J. and Skabar, Y. G.: Synergism between the Low-Level Jet and Organized Convection at Its Exit
1134 Region, *Monthly Weather Review*, 135(4), 1310–1326, doi:10.1175/mwr3317.1, 2007.

1135 Shapiro, A., Fedorovich, E. and Rahimi, S.: A unified theory for the Great Plains Nocturnal low-level jet, *Journal of*
1136 *the Atmospheric Sciences*, 73(8), 3037–3057, doi:10.1175/jas-d-15-0307.1, 2016.

1137 Smith, E. N., Gebauer, J. G., Klein, P. M., Fedorovich, E. and Gibbs, J. A.: The Great Plains Low-Level Jet during
1138 PECAN: Observed and Simulated Characteristics, *Monthly Weather Review*, 147(6), 1845–1869, doi:10.1175/mwr-
1139 d-18-0293.1, 2019.

1140 [Soares, P. M., Lima, D. C., Semedo, A., Cardoso, R. M., Cabos, W. and Sein, D. V.: Assessing the climate change](#)
1141 [impact on the North African offshore surface wind and coastal low-level jet using coupled and uncoupled regional](#)
1142 [climate simulations, *Climate Dynamics*, 52\(11\), 7111–7132, doi:10.1007/s00382-018-4565-9, 2018.](#)

1143 Stensrud, D. J.: Importance of Low-Level Jets to Climate: A Review, *Journal of Climate*, 9(8), 1698–1711,
1144 doi:10.1175/1520-0442(1996)009<1698:iolljt>2.0.co;2, 1996.

1145 Sullivan, J. T., Rabenhorst, S. D., Dreessen, J., McGee, T. J., Delgado, R., Twigg, L. and Sumnicht, G.: Lidar
1146 observations revealing transport of O₃ in the presence of a nocturnal low-level jet: Regional implications for “next-
1147 day” pollution, *Atmospheric Environment*, 158, 160–171, doi:10.1016/j.atmosenv.2017.03.039, 2017.

1148 Tang, Y., Winkler, J., Zhong, S., Bian, X., Doubler, D., Yu, L. and Walters, C.: Future changes in the climatology of
1149 the Great Plains low-level jet derived from fine resolution multi-model simulations, *Scientific Reports*, 7(1),
1150 doi:10.1038/s41598-017-05135-0, 2017.

1151 Uccellini, L. W., Petersen, R. A., Kocin, P. J., Brill, K. F. and Tuccillo, J. J.: Synergistic Interactions between an
1152 Upper-Level Jet Streak and Diabatic Processes that Influence the Development of a Low-Level Jet and a Secondary
1153 Coastal Cyclone, *Monthly Weather Review*, 115(10), 2227–2261, doi:10.1175/1520-
1154 0493(1987)115<2227:sibaul>2.0.co;2, 1987.

1155 Van de Wiel, B. J., Moene, A. F., Steeneveld, G. J., Baas, P., Bosveld, F. C. and Holtslag, A. A.: A conceptual view
1156 on inertial oscillations and nocturnal low-level jets, *Journal of the Atmospheric Sciences*, 67(8), 2679–2689,
1157 doi:10.1175/2010jas3289.1, 2010.

1158 Walters, C. K. and Winkler, J. A.: Airflow Configurations of Warm Season Southerly Low-Level Wind Maxima in
1159 the Great Plains. Part I: Spatial and Temporal Characteristics and Relationship to Convection, Weather and
1160 Forecasting, 16(5), 513–530, doi:10.1175/1520-0434(2001)016<0513:acowss>2.0.co;2, 2001.

1161 Walters, C. K., Winkler, J. A., Shadbolt, R. P., van Ravensway, J. and Bierly, G. D.: A Long-Term Climatology of
1162 Southerly and Northerly Low-Level Jets for the Central United States, *Annals of the Association of American*
1163 *Geographers*, 98(3), 521–552, doi:10.1080/00045600802046387, 2008.

1164 Weide Luiz, E. and Fiedler, S.: Spatiotemporal observations of nocturnal low-level jets and impacts on wind
1165 power production, *Wind Energy Science*, 7(4), 1575–1591, doi:10.5194/wes-7-1575-2022, 2022.

1166 Zhang, Y., Xue, M., Zhu, K. and Zhou, B.: What is the main cause of diurnal variation and nocturnal peak of summer
1167 precipitation in Sichuan Basin, China? the key role of boundary layer low-level jet inertial oscillations, *Journal of*
1168 *Geophysical Research: Atmospheres*, 124(5), 2643–2664, doi:10.1029/2018jd029834, 2019.

1169 Zhong, S., Fast, J. D. and Bian, X.: A Case Study of the Great Plains Low-Level Jet Using Wind Profiler Network
1170 Data and a High-Resolution Mesoscale Model, *Monthly Weather Review*, 124(5), 785–806, doi:10.1175/1520-
1171 0493(1996)124<0785:acsotg>2.0.co;2, 1996.

第 8 页: [1] 删除了

Ma, Xiao

2024/4/29 20:07:00

第 8 页: [1] 删除了

Ma, Xiao

2024/4/29 20:07:00

第 8 页: [1] 删除了

Ma, Xiao

2024/4/29 20:07:00

第 8 页: [1] 删除了

Ma, Xiao

2024/4/29 20:07:00

第 8 页: [1] 删除了

Ma, Xiao

2024/4/29 20:07:00

第 8 页: [1] 删除了

Ma, Xiao

2024/4/29 20:07:00

第 8 页: [1] 删除了

Ma, Xiao

2024/4/29 20:07:00